DIRECTIVITY ENHANCEMENT OF 60 GHZ MICROSTRIP PATCH ANTENNAS USING DIELECTRIC FABRY-PEROT RESONATORS

A THESIS SUBMITTED TO

THE GRADUATE SCHOOL OF

ENGINEERING AND NATURAL SCIENCES

OF ISTANBUL MEDIPOL UNIVERSITY

IN PARTIAL FULFILLMENT OF THE REQUIREMENTS FOR

THE DEGREE OF

MASTER OF SCIENCE

IN

ELECTRICAL, ELECTRONICS ENGINEERING AND CYBER SYSTEMS

By

Müberra Arvas

November, 2019

ABSTRACT

DIRECTIVITY ENHANCEMENT OF 60 GHZ MICROSTRIP PATCH ANTENNAS USING DIELECTRIC FABRY-PEROT RESONATORS

Müberra Arvas
M.S. in Electrical, Electronics Engineering and Cyber Systems
Advisor: Prof. Dr. Ercümend Arvas
November, 2019

The 60 GHz frequency band offers many opportunities for innovations in the wireless network technology, unlike other bands. Since the wavelength in the 60 GHz band is millimetric, this band can suitably represent the line-of-sight LoS part of the wireless communication. It offers superior features in inter-building, near-point and point-to-point wireless networking applications. Nevertheless, and despite its superior properties, this band is prone to a highly effective attenuation in the terrestrial plane (sea level). The reason for this attenuation is that the gases in the atmosphere absorb the signals, especially the coercive behavior of the oxygen molecule around its resonance line in the 60 GHz frequency band. This phenomenon, called oxygen weakening, is the most important drawback that this band suffers. Ironically, this attenuation might be seen as an advantage because it allows reuse of the frequency channels. This thesis is concerned with the propagation of electromagnetic waves in the 60 GHz frequency band from two distinct aspects. First, an attempt to physically model the atmospheric absorption is made. This objective has been achieved by developing a new material model for the atmosphere based on Lorentz functions. The developed model is by far more superior, and more useful, than the existing empirical model. Whereas the applicability of the empirical equations are very limited to ray-tracing propagation methods, the physical model developed in this thesis enjoys unlimited applicability in propagation problems involving the atmosphere because it can be easily incorporated in most electromagnetic simulators. A home-grown time-domain simulation algorithm based on the time-domain finite-difference method (FDTD) has been built and quantitatively tested. In the second part of the thesis, the directivity enhancement of a basic patch antenna which operates at 60 GHz is addressed. Enhancing the directivity of the antenna is an effective design strategy in LoS communication links to overcome channel loss caused by the atmosphere.

A design based on the Dielectric Fabry-Perot Resonator (DFPR) has been developed. Extensive parametric studies on the resonator operation and its effect on the antenna directivity have been performed using a commercial software. When the results are examined, it is shown that the best directivity of the DFPR-based patch antenna is obtained when the antenna resonance is matched to the DFPR resonance. Other design guidelines were also identified and explained. The work done in this thesis opens several directions for further research on different fronts including the atmospheric propagation model as well as directivity enhancement. Possible extensions can be in the range of applicability of the time-domain propagation model as well as the effect of dielectric resonators built around the patch antenna.

Keywords: 60 GHz, microstrip patch antennas, patch antennas, inset-fed, inset-fed patch antennas, absorption, oxygen absorption, FDTD, Lorentz Model, Fabry Perot Theory, Fabry Perot Antenna, dielectric Fabry Perot antennas, directivity, directivity enhancement.

ÖZET

60 GHZ BANDINDA DİELEKTRİK FABRY PEROT YANKILAYICILARININ KULLANILMASIYLA MİKROŞERİT YAMA ANTENLERİN YÖNLÜLÜKLERİNİN ARTTIRILMASI

Müberra Arvas
Elektrik-Elektronik Mühendisliği ve Siber Sistemler, Yüksek Lisans
Tez Danışmanı: Prof. Dr. Ercümend Arvas
Kasım, 2019

60 GHz frekans bandı, diğer bantlardan farklı olarak, kablosuz ağ teknolojisindeki yenilikler için birçok fırsat sunar. 60 GHz bandındaki dalga boyu milimetrik olduğundan, bu bant uygun şekilde kablosuz iletişimin görüş hattı LoS bölümünü temsil edebilir. Binalar arası, yakın-noktaya ve noktadan noktaya kablosuz ağ uygulamalarında üstün özellikler sunar. Bununla birlikte, ve üstün özelliklerine rağmen, bu bant karasal düzlemde (deniz seviyesi) oldukça etkili bir zayıflamaya eğilimlidir. Bu zayıflamanın nedeni, atmosferdeki gazların sinyalleri emmesidir, özellikle oksijen molekülünün 60 GHz frekans bandında rezonans hattı etrafındaki zorlayıcı davranışıdır. Oksijen zayıflaması denilen bu fenomen, bu bandın karşılaştığı en önemli dezavantajdır. Tezat olarak, bu zayıflama, frekans kanallarının tekrar kullanılmasına izin verdiği için bir avantaj olarak görülebilir. Bu tez 60 GHz frekans bandındaki elektromanyetik dalgaların iki farklı yönden yayılımı ile ilgilidir. İlk olarak atmosferik soğurmayı fiziksel olarak modelleme denemesi yapılmıştır. Bu amaca, Lorentz fonksiyonlarını temel alan atmosfer için yeni bir materyal modeli geliştirilerek ulaşıldı. Geliştirilen model, mevcut ampirik modelden çok daha üstündür, ve daha kullanışlıdır. Ampirik denklemlerin uygulanabilirliği ışın-izleme yayılım yöntemleriyle çok sınırlı olsa da, bu tezde geliştirilen fiziksel model atmosferi içeren yayılma problemlerinde sınırsız uygulanabilirliğe sahiptir çünkü çoğu elektromanyetik simülatöre kolayca dahil edilebilir. Sonlu farklar zaman alanı yöntemine (FDTD) dayalı yerli bir zaman-bölge simülasyon algoritması oluşturulmuş ve nicel olarak test edilmiştir. Tezin ikinci bölümünde, 60 GHz'de çalışan temel yama anteninin yönlülük artırımı ele alınmıştır. Antenin yönlendiriciliğinin arttırılması, LoS iletişim bağlantılarında atmosferden

kaynaklanan kanal kaybının üstesinden gelmek için etkili bir tasarım stratejisidir. Dielektrik Fabry-Perot yankılayıcısına dayanan bir tasarım geliştirilmiştir. Rezonatörün çalışması ve anten yönlülüğü üzerindeki etkisi üzerine kapsamlı parametrik çalışmalar ticari bir yazılım kullanılarak yapılmıştır. Sonuçlar tetkik edildiğinde, DFPR temelli yama antenin en iyi yönlülüğünün, anten resonansı DFPR rezonansıyla eşleştiğinde elde edildiğini göstermektedir. Diğer tasarım kılavuzları da tanımlanmış ve açıklanmıştır. Bu tezde yapılan çalışmalar atmosferik yayılım modelleme ve yönlülüğün arttırımı dahil olmak üzere farklı cihetlerde daha ileri araştırmaların yapılması için bir çok kapı açmaktadır. Bu tez konusuna dair olası eklemeler, zaman-bölge yayılımı modelinin uygulanabilirlik aralığı ile yama anteninin etrafına yerleştirilmiş dielektrik rezonatörlerin etkisi olabilir.

Anahtar sözcükler: 60 GHz, mikroşerit yama antenler, yama antenler, ilave-besleme, içe doğru besleme, ilave-beslemeli yama anten, soğurma, emilim, oksijen soğurması, FDTD, Lorentz Modeli, Fabry Perot Teoremi, Fabry Perot Anteni, dielektrik Fabry Perot antenleri, yönlülük, yönlülük geliştirme.

Acknowledgement

I would like to first thank to my thesis advisor Prof. Dr. Ercümend Arvas for his guidance and support despite his busy schedule throughout my study. I would also like to express my gratitude to Prof. Dr. Mohammad Alsunaidi for steering me in the right direction and his compassion during the process of writing my thesis. Their doors were always open for me whenever I need guidance.

I am indebted to Dr. Serhend Arvas, and Assoc. Prof. Dr. Mehmet Kemal Özdemir for their helpful comments. I would like to thank to the director Assoc. Prof. Dr. Yasemin Yüksel Durmaz and to the staffs Erol Akçay, and Hasan Duman of Graduate School of Engineering and Natural Sciences of Istanbul Medipol University for their patience and kindness respectively. I would like to thank to Prof. Dr. Ömer Akgiray, Asst. Prof. Dr. Alper Şişman, and Assoc. Prof. Dr. Fulya Çallıalp of Electrical Electronics Engineering at Marmara University for welcoming me in Marmara University. I would also like to thank to all colleagues and the secretary of Engineering and Electronics Department of Kemal Yuksek at Marmara University. I would like to thank to Muzaffer Kiraz, Hüseyin Anıtkar, Soydan Çakır, Osman Çerezci, Savaş Acak, Bahadır Tektaş from TUBITAK Informatics and Information Security Research Center Antenna Test and Research Laboratory and National Metrology Institute for providing me with the necessary instructions during the antenna measurements. I thank to Dr. Haji M Furqan Madni, and i appreciate all the useful comments of Dr. Orçun Kiriş. I thank to Said Güler for LPKF training. I am thankful to Me'va Önyurt for her kindness and positive comments. Thanks to my kind friends, the Duncan family, for welcoming me in Atlanta when i participated in IEEE APS-URSI 2019 Conference.

I must express my gratitude to my parents for supporting me in reaching my goals. I am grateful to Oksuzomer, Bilici and Erdogan families and to my friends who encouraged me when I needed most. Finally, I would like to thank TUBITAK for supporting me under the project number 215E316.

To my mother and to valuable ladies Tenzile and Fazilet...

Contents

List of Figures

List of Tables

Chapter 1

INTRODUCTION

The demand for fast data transfer and large bandwidth is expected to grow further and further over the coming decades. This is in part due to the large number of applications that require real-time communications and processing, and in part due to extension of costumer expectations and demand. The fact that the unlicensed 60 GHz frequency band is a strong contender to satisfy such demands requires addressing important issues and challenges pertinent to this band. In this chapter, important background on these issues and challenges are discussed, and a short review of the relevant literature on this subject is presented.

1.1 Highlights of Antenna Research at 60 GHz Band

Wireless communication that plays an important role with its mobility and flexibility, has close to 3.5 billion users today and it is expected to increase hundreds of times in the near future. These applications use short-range Gbps technologies and provide hundreds of Mbps transmission capacity [1]. Considering that, home and office environments will also be affected by the world of wireless communication in the near future, the need for the systems that support these applications

is urgent.

Wireless communication, which has become inevitable in our daily lives, plays a very critical role because it offers adaptivity, convenience and mobility. In the long term, it is estimated that the 10 GHz band will not be able to meet excessive demand, and that by 2021 the monthly smartphone traffic will be over 50 petabytes [2]. With the growing population and the use of broadband, the efficiency demands expected from wireless networks are increasing. Considering the number of subscribers and their prevalence in the application, larger network capacity is required. Increasing the capacity can either be done by increasing the bandwidth, spectral efficiency or both. The band expansion approach is not suitable for frequency bands that are already very crowded [3]. An ISM band, 2 GHz, cannot accommodate an 80 MHz channel, while the 5 GHz band can support up to three 160 MHz channels [4]. Wireless data traffic is increasingly pointing towards newer generations of communications systems, where operating frequency is shifting from 2.4/5.8 GHz to 28 GHz and 38 GHz [5]. The 60 GHz band is expected to have data speeds above 1 Gbps in order to provide high-speed internet access, and wireless HDTV. The mobile network connection speed, which was 1 Mbps in previous years, will increase to 16.2 Mbps by 2020 [6]. Nowadays, in addition to the increase in the number of electronic devices, the need for broadband multimedia applications is increasing, which requires the development of wireless systems utilizing short distance data transmission. Indoor band communication has become a part of our lives. This accelerates the usage of millimeter-wave RF communication. In order to ensure high data transmission, the systems should operate in the 57-64 GHz band in the future [7]. In the light of this prediction the 60 GHz frequency band can be a rescuer that meets needs of high-speed data transmission.

The absorption of oxygen of electromagnetic radiation peaks at the 57-64 GHz frequency band. In particular, attenuation of the 60 GHz band at atmospheric conditions is quite high. Because internal and external channels show multi-path behavior, an opportunity for the spatial reuse of the channels is created [1]. This facilitates the re-use of high frequency channels, and thus, high density

is achieved [8]. Thus, it makes communications around the 60 GHz band suitable for the mega-gigabit wireless data transmission [9]. This high attenuation reduces the coverage area and causes the frequency handoffs in the mobile terminals. Besides high attenuation, 60 GHz channels have other challenges, such as non-suitability for non-line-of-sight (NLOS) propagation. Another challenge is having limitations associated with high temperature noise. In addition to these limitations, the spread of 60 GHz signal can be restricted by the mobility of people in the environment, complex terrain and the presence of vehicles, furniture and walls [1].

The main advantage of the 60 GHz frequency band is that it is an unlicensed spectrum that has wide bandwidth. The sizes of antennas are quite small at 60 GHz due to the wavelength decrease. Therefore, this frequency band is compatible with the use of array antenna concept and enables to design numerous sophisticated interfaces. This makes the 60 GHz attractive for indoor networks. Increased number of array elements allows highly directed beams with small variations. The fact that this band has low interference with other networks and low human body skin penetration are other distinct positive aspects [4].

1.2 Atmospheric Absorption

Expectations and demands of the users are increasing with the development of technology. Increased expectations increase interest in unused frequency bands. In order to offer more bandwidth to users, Ka, Ku and EHF bands are being utilized. In the mm-wave band, the wavelength is in the range of 1-10 mm. These bands are known for having wider bandwidth and higher data rate. Propagation problems are important for each band and increase as frequency increases. Atmospheric attenuation is the reduction of an acoustic or electro-magnetic signal due to gases in the atmosphere as it propagates. For millimeter-wave propagation, atmospheric attenuation is very important. This weakening may be caused by gases in the atmosphere as well as weather conditions, such as in rainy and foggy weather.

The H_2O and O_2 are the major molecular absorbers and the absorption occurs with the help of the stimulation of rotational transitions. The size of the electrical dipole moment of the molecule is the main factor in determining the strength of molecular absorption. This dipole moment is weaker in oxygen molecules than in water molecules. However, it is not the strength of the dipole moment that makes the oxygen absorption high but its large concentration in the atmosphere [10]. A review of atmospheric conditions effect in the presence of rain is proposed in [11]. Other factors that are also reviewed in [11] include fog, oxygen, water vapor, cloud, and temperature factors. The analog signal is quantized and a millimeter wave carrier is used for transmission over an antenna. By using the wobulation technique [12] less erroneous data are received at the receiver. Wobulation means wobble in characteristic or change in characteristic. This technique has been used to increase the likelihood of obtaining accurate information in the presence of rain. In this way, successive transmission of data is provided.

1.3 Patch Antenna Directivity

The concentration of the energy at a certain direction is called directivity. Directivity and power gain have the same value when the antenna efficiency is 100%. The power gain expression is usually given in terms of a reference, such as a half-wavelength dipole or an isotropic radiator. The following analysis follows [13].

The radiated power of an antenna can be expressed as

$$P = \int\int \mathbf{S}.d\mathbf{s} = \frac{1}{2} Re \int\int \mathbf{E} \times \mathbf{H}^*.d\mathbf{s} \tag{1.1}$$

where P, $\mathbf{S}$, $\mathbf{E}$ and $\mathbf{H}$ are the power radiated, Poynting vector, electric field intensity, and magnetic field intensity vectors, respectively. Or, using electric and magnetic field components in spherical coordinates,

$$P = \frac{1}{2} Re \int_0^{2\pi} \int_0^{\pi} (E_\theta H_\varphi \times E_\varphi H_\theta^*) r^2 sin\theta d\theta d\phi \tag{1.2}$$

Substituting $H_\varphi = \frac{E_\theta}{\eta}$ and $H_\theta = -\frac{E_\varphi}{\eta}$ in 1.2

$$P = \frac{1}{2\eta} Re \int\int (|E_\theta|^2 + |E_\varphi|^2) r^2 d\Omega \tag{1.3}$$

where $d\Omega = sin\theta d\theta d\varphi$ is the element of solid angle, and η is characteristic impedance.

The radiation intensity is given by;

$$U(\theta, \varphi) = \frac{1}{2} Re(E \times H^*).r^2 \mathbf{r} = S(\theta, \varphi) r^2 \tag{1.4}$$

$$U(\theta, \varphi) = U_m \mid F(\theta, \varphi) \mid^2 \tag{1.5}$$

where, U_m is the maximum radiation intensity. $\mid F(\theta, \varphi) \mid^2$ is the power pattern normalized to a maximum value of unity in the direction $(\theta_{max}, \varphi_{max})$

Thus, total power radiated becomes

$$P = \int\int U(\theta, \varphi) d\Omega = U_m \int\int \mid F(\theta, \varphi) \mid^2 d\Omega \tag{1.6}$$

$$P = \int\int U_{ave} d\Omega \tag{1.7}$$

$$P = U_{ave} \int\int d\Omega = 4\pi U_{ave} \tag{1.8}$$

For non-isotropic sources U_{ave} is given by

$$U_{ave} = \frac{1}{4\pi} \int\int U(\theta, \varphi) d\Omega = \frac{P}{4\pi} \tag{1.9}$$

Consider an ideal half wavelength dipole, the above quantities become

$$U(\theta, \varphi) = \frac{1}{2} (\frac{I\Delta z}{4\pi})^2 \beta\omega\mu sin^2\theta \tag{1.10}$$

$$U_m = \frac{1}{2} (\frac{I\Delta z}{4\pi})^2 \beta\omega\mu \tag{1.11}$$

$$F(\theta, \varphi) = sin(\theta) \tag{1.12}$$

The average radiation intensity follows from the total radiated power expression eq. 1.13 for an ideal dipole as

$$U_{ave} = \frac{P}{4\pi} = \frac{(\frac{\beta\omega\mu}{12\pi})(I \triangle z)^2}{4\pi} = \frac{1}{3}(\frac{I \triangle z}{4\pi})^2 \beta\omega\mu = 2/3U_m \tag{1.13}$$

Thus $U_m = 1.5U_{ave}$ for the ideal dipole, which means that, in the direction of maximum radiation, intensity is 50 % more than that of an isotropic source radiating the same total power.

Directivity is defined as the ratio of radiation intensity to the average radiation intensity, as

$$D(\theta, \phi) = \frac{U(\theta, \phi)}{U_{ave}} \tag{1.14}$$

Dividing the denominator by r^2, then the power densities and the directivity become

$$D(\theta, \phi) = \frac{U(\theta, \phi)r^2}{U_{ave}(\theta, \phi)} = \frac{\frac{1}{2}Re(E \times H^*).\widehat{r}}{\frac{P}{4\pi r^2}} \tag{1.15}$$

Or,

$$D(\theta, \phi) = \frac{U(\theta, \varphi)}{1/4\pi \int\int U(\theta, \varphi) d\Omega} = \frac{|F(\theta, \varphi)|^2}{4\pi \int\int |F(\theta, \varphi)|^2 d\Omega} = \frac{4\pi}{\Omega_A}|F(\theta, \varphi)|^2 \tag{1.16}$$

1.4 Electromagnetic Simulators

In recent years, many universities started requiring students specializing in the field of electromagnetics (EM) to develop skills in computational analysis. This learning outcome is partly achieved by teaching the students the basics of numerical analysis and partly by training on commercial solvers. This subject has been traditionally called "*Computational Electromagnetics*" (CEM). It helps future scientists and engineers become proficient in one or more of the commercial electromagnetic simulators. These simulators are mostly based on the three well-known methods, the *finite element method* (FEM), the *method of moments* (MoM) and the *finite difference time domain method* (FDTD). Examples of popular simulators include HFSS (FEM), COMSOL RF Module (FEM), FEKO (MoM) and XFDTD (FDTD).

Commercial simulators have so far succeeded in the analysis of many standard and, sometimes complex, electromagnetic problems. However, in certain situations, it is necessary to develop specialized simulation algorithms to obtain the desired solution. For example, in situations where Maxwell's equations are modified to include a specific material behavior or when auxiliary equations are solved concurrently with the basic Maxwell's or wave equations. Another example is when one or more media within the computational domain possess non-standard material models. In these situations, either open-source software (such as FDTD-based EM software package MEEP [14] from Massachusetts Institute of Technology), or a home-grown software is developed.

The work in this thesis involves both scenarios; the antenna analysis will be carried out using a commercial simulator (COMSOL), whereas the atmospheric propagation analysis will be carried out by a home-grown FDTD simulator. In the following paragraphs, brief introductions to COMSOL and the FDTD method are given.

COMSOL [15], is a simulation environment in which real applications can be designed and analyzed. The goal of the simulation is to carry and observe the effects in this environment. COMSOL, is a multi-physics program that allows presenting all of these effects from the real world in a simulation environment. This allows scientists and engineers to elaborate their discoveries and produce innovative solutions to problems. COMSOL, will also develop in the future with very effective results in real world applications and will contribute to inspiring works.

The main features of this simulator are as follows.

- COMSOL can be easily integrated into many programs such as MATLAB.
- It is a FEM-based analysis program.
- Automatic report writing feature is available.
- It is possible to enter parametric geometry.

- Predefined physics interfaces make the model creation process quick and practical.
- At each stage, there is the chance to add a different physics to the problem.
- The equations can be expanded and moved to advanced levels depending on the needs.
- Available modules up to now are: Acoustic Module, Batteries Fuel Cells Module, CAD Import Module, Corrosion Module, CFD Module, Chemical Reaction Engineering Module, Design Module, Electrochemistry Module, ECAD Import Module, Fatigue Module, Heat Transfer Module, Geomechanics Module, MEMs Module, Microfluidics Module, Mixer Module, Optimization Module, Plasma Module, Ray Optics Module, RF Module, Semiconductor Module and Wave Optics Module.

The finite difference time domain numerical technique has become one of the well known numerical technique to solve propagation problems not only in the field of electromagnetics but also in many fields of engineering. It gained a huge boost when a new grid arrangement was introduced by Kane Yee in 1966 for the numerical solution of Maxwell's equations [16]. This method uses finite differences to approximate the spatial and temporal derivatives. Over the years, it improved exponentially with several advanced models and algorithms and has become a method of choice in computational tools to solve complex time-domain electromagnetic problems. The continuous research and development in this field have led to more efficient and stable numerical algorithms to solve EM problems covering a wide range of applications, from static and low-frequency analysis to nano-photonics. The main topics where FDTD method finds application are as follows.

- Military defense applications: Antennas and circuits, radar technologies, improvement of high-power microwave sources.
- Semiconductor devices including electronic devices and circuits and microwave components.

- Photonic and nanophotonic structures, devices, circuits and components.
- Bio-electromagnetic simulations of bio-medical devices and phenomena.
- High speed communication links and systems.

The main advantages of the FDTD method can be summarized in the following.

- The development of the FDTD algorithm is simple due to the nature of the derivative approximation.
- The algorithm is robust as a huge wealth of information can be extracted from a single run.
- It is a well-developed technique with lots of improvements and add-ons, such as hybrid grids and multi-scales, making it suitable to be tailored for the analysis of electromagnetic problems in research and in industry.
- It can be utilized in a wide spectrum of EM problems including from ultra low to ultra high frequencies.
- It can produce results for multi-wavelength propagations in one run.
- It provides a satisfactory analyze capability with the well-established absorbing/periodic/rotating/moving and other boundary conditions for all situations encountered in EM problems.
- It is naturally suited for implementation on parallel machines.
- Specific material and multi-physical models can be easily incorporated in the main algorithm using auxiliary equations extending its application to new materials and new phenomena.

The main disadvantages of the FDTD method can be summarized in the following.

- The FDTD method is explicit in nature and prone to numerical dispersion. Consequently, the computational cost increases with finer mesh sizes.
- The spatial steps are governed by the amount of numerical dispersion (i.e., accuracy).
- The time step is, in general, limited by Courant- Friedrich- Levy (CFL) stability criterion [17].
- The curved boundaries are poorly represented.

The formulation of an FDTD-based solution of Maxwell's equations is developed as follows. Consider a non-dispersive, linear, isotropic and source-free case, Maxwell's equations are written as

$$\frac{\partial \mathbf{H}}{\partial t} = -\frac{1}{\mu}\nabla \times \mathbf{E} \tag{1.17}$$

$$\frac{\partial \mathbf{E}}{\partial t} = \frac{1}{\varepsilon}\nabla \times \mathbf{H} \tag{1.18}$$

Following six coupled equations are obtained by expanding the eq. 1.17 and eq. 1.18

$$\frac{1}{\mu_x}(\frac{\partial E_z}{\partial y} - \frac{\partial E_y}{\partial z}) = -\frac{\partial H_x}{\partial t} \tag{1.19}$$

$$\frac{1}{\mu_y}(\frac{\partial E_x}{\partial z} - \frac{\partial E_z}{\partial x}) = -\frac{\partial H_y}{\partial t} \tag{1.20}$$

$$\frac{1}{\mu_z}(\frac{\partial E_y}{\partial x} - \frac{\partial E_x}{\partial y}) = -\frac{\partial H_z}{\partial t} \tag{1.21}$$

$$\frac{1}{\varepsilon_x}(\frac{\partial H_z}{\partial y} - \frac{\partial H_y}{\partial z}) = -\frac{\partial E_x}{\partial t} \tag{1.22}$$

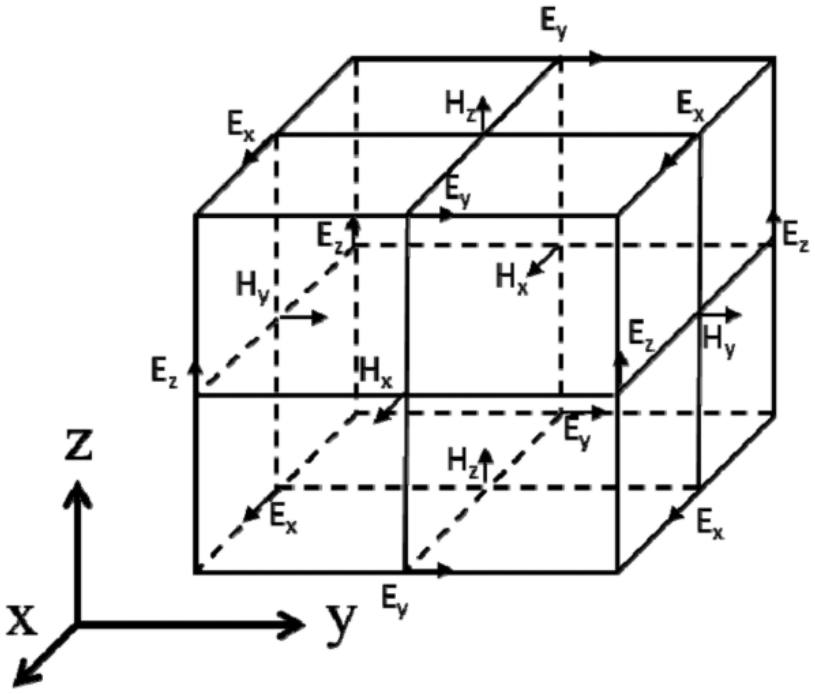

Figure 1.1: The Yee's Mesh

$$\frac{1}{\varepsilon_y}\left(\frac{\partial H_x}{\partial z} - \frac{\partial H_z}{\partial x}\right) = -\frac{\partial E_y}{\partial t} \tag{1.23}$$

$$\frac{1}{\varepsilon_z}\left(\frac{\partial H_y}{\partial x} - \frac{\partial H_x}{\partial y}\right) = -\frac{\partial E_z}{\partial t} \tag{1.24}$$

According to the Yee's orthogonal mesh, the arrangement of the electric and magnetic field components is such that they are staggered in both time and space. The adjustments of compenents are shown in Fig. 1.1. Every H component is hemmed in by four E components. The mesh provides a practical and proper use of central differences for second order algorithm without any discrepancies. Likewise both fields are set up in time domain.

For simplicity, a one-dimensional propagation along the x direction is considered. Eqs. 1.17-1.18 reduce to

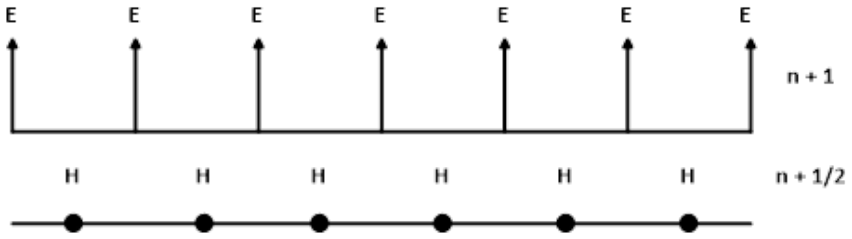

Figure 1.2: Time domain illustration of the Yee's algorithm.

$$\frac{\partial \mathbf{E}_y}{\partial t} = -\frac{1}{\varepsilon}\frac{\partial \mathbf{H}_z}{\partial x} \tag{1.25}$$

$$\frac{\partial \mathbf{H}_y}{\partial t} = \frac{1}{\mu}\frac{\partial \mathbf{E}_z}{\partial x} \tag{1.26}$$

The one-dimensional version of the Yee's mesh is shown in Fig. 1.2. The above equations are now discretized by utilizing the central difference approximation for the first order partial derivatives as follows.

$$\frac{E_y^{n+1}(i_1) - E_y^n(i)}{\Delta t} = -\frac{1}{\varepsilon}\frac{H_z^{n+1/2}(i+1/2) - H_z^{n+1/2}(i-1/2)}{\Delta x} \tag{1.27}$$

$$\frac{H_z^{n+1/2}(i+1/2) - H_z^{n-1/2}(i-1/2)}{\Delta t} = \frac{1}{\mu}\frac{E_y^n(i+1) - E_y^n(i)}{\Delta x} \tag{1.28}$$

The upper limit of time step Δt is specified by the Courant-Friedrich-Levy (CFL) criterion to ensure the stability of the algorithm [17]. In a three-dimensional situation, it is given as

$$\Delta t \leq \Delta t_{max} = \frac{1}{\upsilon_{max}\sqrt{(\frac{1}{\Delta x^2}) + (\frac{1}{\Delta y^2}) + (\frac{1}{\Delta z^2})}} \tag{1.29}$$

where, υ_{max} represents the maximum velocity of EM waves in the medium. This is the only stability requirement for the proper use of the FDTD method. The determination of the spatial cell size varies according to the problem to be solved.

For the majority of applications, the general guideline is to make the spatial step a very small fraction of the smallest wavelength involved in the propagation (e.g., $\lambda_{min}/40$).

1.5 Thesis Goals, Objectives and Methodology

The main goals of this study are to provide a quantitative approach to the accurate calculations of atmospheric absorption at the 60 GHz frequency band, and to propose a possible method for overcoming this loss by improving the antenna directivity. These two main goals are achieved using a combination of analytical, modeling and simulation techniques. Analytical techniques include the derivation of the atmospheric material model at the 60 GHz frequency band and the design of the Fabry-Perot cavity. The simulation techniques include the incorporation of the atmospheric frequency-domain model into a time-domain simulator. Simulations of the wave propagation are carried out using the finite-difference time-domain method. Additionally, for the analysis and design of the resonator-based patch antenna, simulations using the RF COMSOL module are performed. The main findings of this work have been experimentally verified.

The thesis work achieves a number of specific objectives, as follows:

1. Conduct a comprehensive literature survey on the atmospheric material models at 60 GHz frequency band that are suitable to incorporate in standard electromagnetic simulators, evaluate these models and suggest possible improvements.

2. Collect reliable measurement data on atmospheric absorption in the 60 GHz frequency band. The data will be useful in the development of a frequency-dependent material model.

3. Develop a frequency-dependent material model for the atmosphere at the 60 GHz frequency band. The model should be put in standard material models

(generally Lorentzian) to be incorporated in time-domain simulators (e.g., FDTD method).

4. Build, test and validate a time-domain simulator for the propagation of electromagnetic waves in the 60 GHz frequency band through sea-level atmosphere.

5. Conduct an extensive literature survey on patch antenna designs for the 60 GHz frequency band. Identify the techniques used to improve antenna performance, especially directivity.

6. Study and design a basic dielectric Fabry-Perot-based resonator (FPR) to be incorporated within the antenna environment. Specify the different parameters that potentially affect the antenna directivity.

7. Perform simulations and parametric studies on the DFPR to arrive at the best design candidates.

8. Verify the basic concepts experimentally.

9. Draw concrete conclusions on all findings of the work and give recommendations for further research.

1.6 Thesis Organization

Organization of this thesis is described briefly below.

Chapter 1 presents a conspectus of the challenges that communication links utilizing the 60 GHz frequency band face including challenges related to atmospheric absorption and those related to antenna design. A detailed literature review outlining the approaches and techniques that have been so far used to meet these challenges is presented. The chapter also describes the goals and objectives of this thesis. Chapter 2 focuses on atmospheric absorption and gives elaborated development of a novel material model for the atmosphere at the 60 GHz frequency band. It also shows the incorporation process of the developed

material model in the FDTD method. Numerical experiments of wave propagation through the atmosphere are presented and the results are validated.

Chapter 3 provides a brief description of the theory of Fabry-Perot resonators. This background is necessary for the design of the DFPR that is incorporated in the antenna design. Chapter 4 presents extensive simulations and parametric studies on the DFPR antenna design. It studies the most important factors that contribute to the enhancement of antenna directivity.

Chapter 5 covers summary, contribution of thesis and conclusions. Additionally represents the possible extensions for the presented work.

Chapter 2

ANALYSIS OF ATMOSPHERIC ABSORPTION AT 60 GHZ

At 60 GHz, electromagnetic waves are strongly weakened by the gases in the atmosphere. Quantitative analysis of the atmospheric attenuation of waves is very essential for the proper design and positioning of radiating elements. Beside antenna design, an accurate simulation model should find applications in many disciplines, including remote sensing, geophysical mapping and in point-to-point communications, where it can help in planning the positions of ground and air-borne facilities. In this chapter, a three-fold objective is presented for the atmospheric attenuation modelling. First, an analytical model of atmospheric attenuation is developed by fitting atmospheric measurement data to a standard material model. The model of choice is the Lorentz model because Lorentz functions represent the most general matter-wave interaction forms. Second, the material model is incorporated in the time-domain simulations of Maxwell's equations and specifically in a FDTD algorithm to study wave propagation in the atmosphere. This objective is achieved through the general polarization formulation and the auxiliary differential equation technique (ADE). Finally, simulations of a long-distance propagation of waves in the 60 GHz frequency band are carried out.

2.1 Introduction

The desire on fast data transfer and broadband is increasing in the coming years, partly because of the large number of multimedia applications that require real-time communication and processing, and partly due to increased consumer expectations. The fact that the unlicensed 60 GHz frequency band is a stronger competitor than the other bands to meet these demands requires addressing important issues and challenges associated with 60 GHz frequency band. The sea level atmosphere is known for its significant attenuation of frequencies around 60 GHz due to high oxygen absorption. Oxygen absorption constitutes over 95% of this atmospheric attenuation which peaks around 60 GHz, with a value of over 15 dB/km. The successful adoption of 5G communications using the 60 GHz frequency band for wireless and radio communications relies on the introduction of novel antenna designs and communication strategies to overcome the channel loss. There has been a lot of emphasis on measurement [18, 19] and modeling [20, 21, 22] techniques of atmospheric attenuation. The modeling effort focuses on the precise representation of the physical phenomena involving oxygen absorption lines at different atmospheric conditions. The final product of these models is customarily represented by a large variety of functions and polynomials (empirical fitting) with several physical parameters and mixing coefficients. The resulting empirical models are useful and can be utilized to approximate attenuation levels as a function of frequency and elevation. On the other hand, work has been done on the utilization of these models in solving real-life propagation problems. Grishin et. al. used experimental data for atmospheric signal attenuation in an analytical model based on solving an inverse problem to simulate satellite signal propagation [23]. The work done in [24, 25] simulated the signal absorption and dispersion due to the atmosphere by embedding the empirical relations into a transfer function and placed it in the channel part of the communication system. Other methods based on analytical solutions can in fact utilize these empirical functions but only for the treatment of simple propagation situations. Calculations based on the ray tracing method and the parabolic wave approximation have been proposed [26, 27, 28, 29]. The ray tracing method is more suited for propagation problems with large-size features over a smooth ground in a homogeneous

atmosphere. For complex environments, the computational time drastically increases, and the accuracy deteriorates as the number of required rays significantly increases. Also, the method fails for gazing angles. On the other hand, although the methods based on parabolic approximation are good for large distance propagation, they become less effective in solving problems involving complex terrain and strong atmospheric dispersion. Obviously, because empirical models representing the atmosphere involve complicated expressions and functions, analytical methods become limited in application. Instead, the empirical models need to be incorporated into standard full-wave electromagnetic simulators using, for example, the finite-difference time-domain method and the finite-element method (FEM).

2.2 The ITU Experimental Model

The International Telecommunication Union (ITU) is a United Nations agency founded in 1865, specialized in telecommunication and radio communication that is providing network and services for governments and companies. The ITU is responsible for the development, management and standardization of information and communication technology, though it also provides methods to estimate the attenuation of atmospheric gases on terrestrial and slant paths. A recent gases absorption report [19] provides methods to estimate the attenuation of atmospheric gases on terrestrial and slant paths. The report provides a gas attenuation estimate calculated by summing individual absorption lines for a broad frequency range from 1 GHz to 1 THz. Also given is a simplified approximate method to estimate gaseous attenuation for the frequency range 1-350 GHz. Fig. 2.1 shows the specific atmospheric attenuation curves at different altitudes.

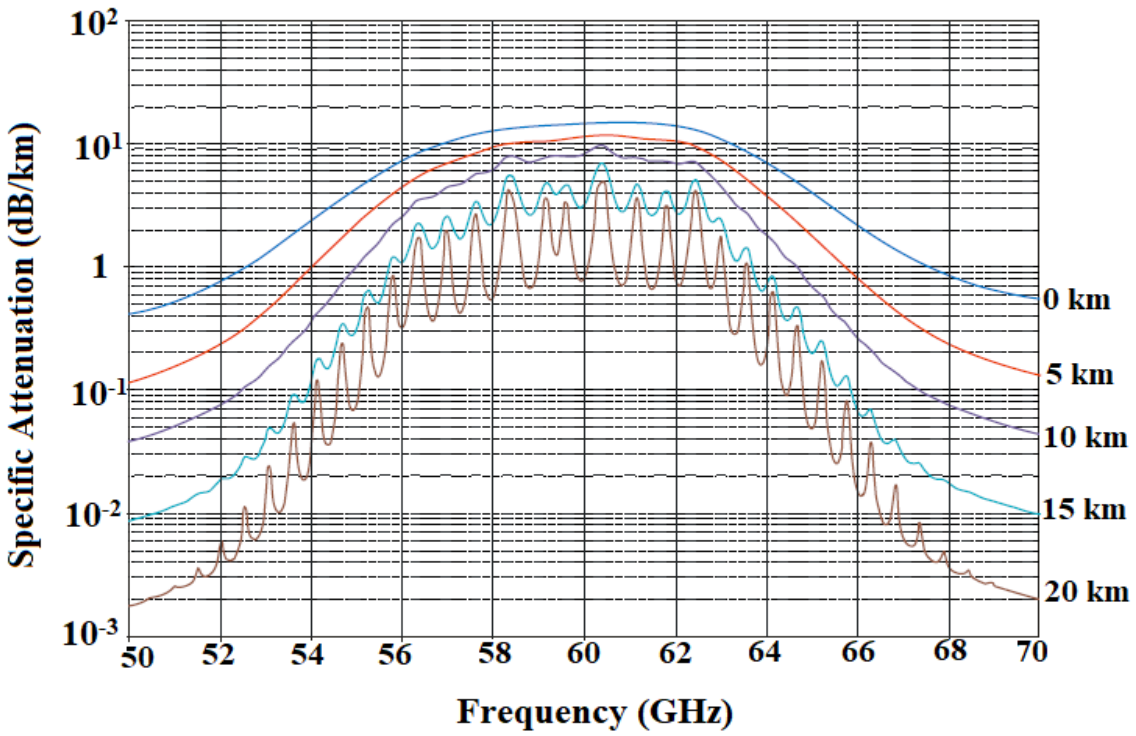

Figure 2.1: The specific attenuation due to atmospheric gases depending on frequency [19].

To be able to use the curves of Fig. 2.1, the ITU report also provides the empirical formulae for the atmospheric attenuation at different frequency intervals. In this thesis, data regarding sea-level propagation is used [19]. The following equations are used, each with the corresponding frequency range. The frequency range of interest is 40-80 GHz.

$f \leq 54$ GHz

$$\gamma_0 = \left[\frac{7.2 r_t^{2.8}}{f^2 + 0.34 r_p^2 r_t^{1.6}} + \frac{0.62 \xi_3}{(54 - f)^{1.16\xi_1} + 0.83\xi_2} \right] f^2 r_p^2 \times 10^{-3} \qquad (2.1)$$

54<$f \leq$ 60 GHz

$$\gamma_0 = exp\left[\frac{ln\gamma_{54}}{24}(f-58)(f-60) + \frac{ln\gamma_{58}}{8}(f-54)(f-60)]\frac{ln\gamma_{60}}{12}(f-54)(f-58)\right] \tag{2.2}$$

60<$f \leq$ 62 GHz

$$\gamma_0 = \gamma_{60} + (\gamma_{62} - \gamma_{60})\frac{(f-60)}{2} \tag{2.3}$$

62<$f \leq$ 66 GHz

$$\gamma_0 = exp\left[\frac{ln\gamma_{62}}{8}(f-64)(f-66) - \frac{ln\gamma_{64}}{4}(f-62)(f-66) + \frac{ln\gamma_{66}}{8}(f-62)(f-64)\right] \tag{2.4}$$

66<$f \leq$ 120 GHz

$$\left[3.02 \times 10^{-}4r_t^{3.5} + \frac{0.283r_t^{3.8}}{(f-118.75)^2 + 2.91r_p^2 r_t^{1.6}} + \frac{0.502\xi_6[1 - 0.0163\xi_7(f-66)]}{(f-66)^{1.4346\xi_4} + 1.15\xi_5}\right] f^2 r_p^2 \times 10^{-3} \tag{2.5}$$

The definitions of the variables ξ , γ , δ , and φ variables are as follows.

$$\xi_1 = \varphi(r_p, r_t, 0.0717, -1.8132, 0.0156, -1.6515) \tag{2.6}$$

$$\xi_2 = \varphi(r_p, r_t, 0.5146, -4.6368, -0.1921, -5.7416) \tag{2.7}$$

$$\xi_3 = \varphi(r_p, r_t, 0.3414, -6.5851, 0.2130, -8.5854) \tag{2.8}$$

$$\xi_4 = \varphi(r_p, r_t, -0.0112, 0.0092, -0.1033, -0.0009) \tag{2.9}$$

$$\xi_5 = \varphi(r_p, r_t, 0.2705, -2.7192, -0.3016, -4.1033) \tag{2.10}$$

$$\xi_6 = \varphi(r_p, r_t, 0.2445, -5.9191, 0.0422, -8.0719) \tag{2.11}$$

$$\xi_7 = \varphi(r_p, r_t, -0.1833, 6.5589, -0.2402, 6.131) \tag{2.12}$$

$$\gamma_{54} = 2.192\varphi(r_p, r_t, 1.8286, -1.9487, 0.4051, -2.8509) \tag{2.13}$$

$$\gamma_{58} = 12.59\varphi(r_p, r_t, 1.0045, 3.5610, 0.1588, 1.2834) \tag{2.14}$$

$$\gamma_{60} = 15.0\varphi(r_p, r_t, 0.9003, 4.1335, 0.0427, 1.6088) \tag{2.15}$$

$$\gamma_{62} = 14.28\varphi(r_p, r_t, 0.9886, 3.4176, 0.1827, 1.3429) \tag{2.16}$$

$$\gamma_{64} = 6.819\varphi(r_p, r_t, 1.4320, 0.6258, 0.3177, -0.5914) \tag{2.17}$$

$$\gamma_{66} = 1.908\varphi(r_p, r_t, 2.0717, -4.1404, 0.4910, -4.8718) \tag{2.18}$$

$$\delta = -0.00306\varphi(r_p, r_t, 3.211, -14.94, 1.583, -16.37) \tag{2.19}$$

$$\varphi(r_p, r_t, a, b, c, d) = r_p^a r_t^b exp[c(1 - r_p) + d(1 - r_t)] \tag{2.20}$$

The parameters used in the equations are, f: frequency (GHz), p: pressure (hPa), T: temperature (°C), $r_p = p/1013$: relative pressure and r_t=288/(273 + T): relative temperature. Fig. 2.2 is a reproduction of the atmospheric specific attenuation using the above empirical formulae for frequencies between 40 and 80 GHz. The atmospheric conditions for the curve in Fig. 2.2 are as follows: dry air, total air pressure of 1033.6 hPa and average temperature of 15 °C.

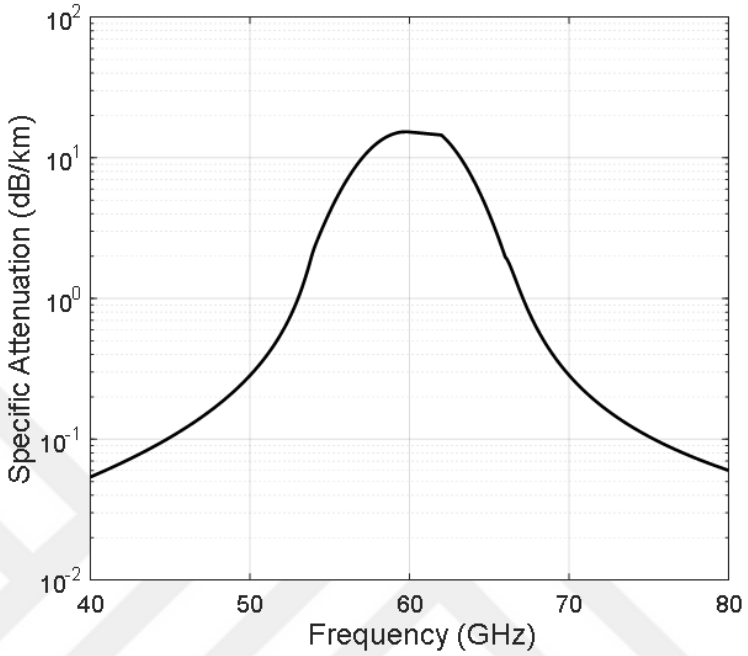

Figure 2.2: Atmospheric specific attenuation for the 40-80 GHz frequency range at sea level, as given by the empirical formulae in [19].

2.3 Dispersive Analytical Material Model for the Atmosphere in the 60 GHz Band

The propagation of electromagnetic waves inside any material, as described by the solution of Maxwell's equations, is affected by the frequency-dependent parameters of the material, such as attenuation and dispersion. Therefore, to account for such effects appropriate models that describe material properties have to be used. In a source-free region, Maxwell's equations are given by

$$\nabla \times \mathbf{H} = \frac{\partial \mathbf{D}}{\partial t} \tag{2.21}$$

$$\frac{\partial \mathbf{B}}{\partial t} = -\nabla \times \mathbf{E} \tag{2.22}$$

$$\nabla . \mathbf{D} = 0 \tag{2.23}$$

$$\nabla . \mathbf{B} = 0 \tag{2.24}$$

where $\mathbf{D}$, $\mathbf{E}$, $\mathbf{B}$ and $\mathbf{H}$ are the electric flux density, electric field intensity, magnetic flux density and magnetic field intensity vectors, respectively. Material properties are described through the constituent relations

$$\mathbf{D}(\omega) = \varepsilon_0 \varepsilon_r(\omega) \mathbf{E}(\omega) \tag{2.25}$$

and

$$\mathbf{B}(\omega) = \mu \mathbf{H}(\omega) \tag{2.26}$$

where μ and ε are, respectively, the permeability and the permittivity of the material. These parameters are, in general, frequency-dependent.

For non-magnetic materials, the electric polarization is used to represent the dielectric effects inside the material. Assuming a linear material response, the frequency-dependent electric flux density, $\mathbf{D}(\omega)$, can be written as

$$\mathbf{D}(\omega) = \varepsilon_0 \varepsilon_\infty \mathbf{E}(\omega) + \mathbf{P}(\omega) \tag{2.27}$$

where, ε_0 is the free space permittivity, ε_∞ is the high frequency dielectric constant and ω is the frequency. The first order linear polarization $\mathbf{P}(\omega)$ is related to the electric field intensity, $\mathbf{E}(\omega)$, in the frequency domain by the electric susceptibility as,

$$\mathbf{P}(\omega) = \varepsilon_0 \chi(\omega) \mathbf{E}(\omega) \tag{2.28}$$

Combining Eqs. 2.27 and 2.28, one can write

$$\varepsilon_r(\omega) = \varepsilon_\infty + \chi(\omega) \tag{2.29}$$

where, $\varepsilon_r(\omega)$ is the frequency-dependent complex relative permittivity of the dispersive material. The dispersion relation for the electric susceptibility $\chi(\omega)$ that represents the material-wave interaction can be derived using the classical electron oscillator (CEO) model [30]. The derivation starts with writing the force

equation which describes the dynamics of the CEO system. Depending on the specific material type (metal, dielectric, etc.), one can arrive at one of the many standard material models (e.g., Debye, Lorentz, Drude, etc.). For the atmosphere case, The Lorentz model is the most suitable, and general, model because it accounts for attenuation, dispersion and resonance.

2.3.1 The Lorentz Material Model

The Lorentz model describes the electron-wave interaction inside a material using the CEO model for any dielectric material. The CEO system can be liken to the spring-mass system. The attitude of electrons in the existence of an external electric field is similar to oscillation of a mass bonded to a spring. As a matter of fact there are no differences between them except that electrons bind to the atomic nucleus. The relation between polarization and electric field is given as [31, 32, 33].

$$\mathbf{P}(\omega) = \frac{ne^2}{m(\omega_0^2 + j\delta\omega - \omega^2)}\varepsilon_0\mathbf{E}(\omega) \tag{2.30}$$

where n is electron density, m is electron mass, e is the electronic charge, ω_0 is the resonance frequency of the system and δ is the damping parameter. The electric susceptibility $\chi(\omega)$ and $\varepsilon_r(\omega)$ are, thus, given by

$$\chi(\omega) = \frac{P(\omega)}{\varepsilon_0 E(\omega)} = \frac{ne^2}{\varepsilon_0 m(\omega_0^2 + j\delta\omega - \omega^2)} \tag{2.31}$$

where $\omega_p^2 = \frac{ne^2}{\varepsilon_0 m}$ and

$$\varepsilon_r(\omega) = \varepsilon_\infty + \frac{ne^2}{\varepsilon_0 m(\omega_0^2 + j\delta\omega - \omega^2)} = \varepsilon_\infty + \frac{\omega_p^2}{\omega_0^2 + j\delta\omega - \omega^2} \tag{2.32}$$

In this thesis, the frequency-dependent relative permittivity of the atmosphere is modeled using a multi-pole Lorentzian function of the form [31, 32, 33]

$$\varepsilon_r(\omega) = \varepsilon_\infty + (\varepsilon_s - \varepsilon_\infty)\sum_{i=1}^{M} \frac{A_i\omega_i^2}{(\omega_i^2 + j2\delta_i\omega - \omega^2)} \tag{2.33}$$

where ε_s is the effective static dielectric constant,A_i is the pole strength, ω_i is the resonance frequency, δ_i is the damping parameter and M is the number of poles.

2.3.2 The Developed Model

For simplicity, the frequency-dependent susceptibility function for a single pole is written as

$$\chi(\omega) = \frac{a}{b + jc\omega - d\omega^2} \tag{2.34}$$

where a, b, c and d are model parameters that can be obtained from material properties or by fitting to experimental data. Unfortunately, the empirical formulae representing the atmospheric behavior are not adequate to be included in a time-domain simulator. So, it is required to put these measurement data into standard material model forms. In this work, a fitting to the general Lorentz poles is performed. The strategy for using the experimental data is as follows. For any given frequency range, elevation and atmospheric conditions, frequency-dependent data for the complex permittivity is obtained from attenuation readings using the following analysis.

The real and imaginary parts of the dielectric constant ε_r are related to the real and imaginary parts of the refractive index n using

$$\varepsilon_r' = (n')^2 + (n'')^2 \tag{2.35}$$

and,

$$\varepsilon_r'' = -2n'n'' \tag{2.36}$$

where a single prime indicates the real part and a double prime indicates the imaginary part. Also, the absorption coefficient α is given by

$$\alpha = \frac{2\omega}{\upsilon} n'' \tag{2.37}$$

where, v is the speed of light inside the medium. This, leads to the following relation

$$\varepsilon_r'' = -\frac{\alpha c n'}{\omega} \tag{2.38}$$

or,

$$\varepsilon_r'' = -\frac{\alpha \upsilon}{\omega} \sqrt{1 - (\frac{\alpha \upsilon}{2\omega})^2} \tag{2.39}$$

where, c is the speed of light in vacuum. Eqs. 2.35 and 2.39 represent the link between the available experimental absorption data and the frequency-dependent

dielectric function. The obtained complex dielectric function data are fitted to standard material models with as many poles as required. Out of the fitting process, the model parameters are obtained. Comparing Eq. 2.33 and Eq. 2.34, the model parameters are given by: $a_i = (\varepsilon_s - \varepsilon_\infty)\omega_i^2$, $b_i = \omega_i^2$, $c_i = 2\delta_i$, and $d_i = 1$.

2.3.3 Two-pole Lorentz Model for the Atmosphere at 60 GHz

The objective here is to fit the obtained dielectric function to a Lorentz function using two poles. The fitting process to Lorentzian poles goes as follows. One can start with a Lorentzian pole that has a peak around the center of the curve in Fig. 2.2 (i.e., around 60 GHz). This step yields the value of the resonance frequency of the first pole. Next, to accommodate for the width of the spectrum of the measurements data, other poles at above and below the first resonance frequency are added. Finally, the values of the pole strength and damping parameter for each pole are adjusted such that a reasonable fit is obtained. Table 2.1 shows the a, b, c and d parameters for the two Lorentz poles used for atmospheric attenuation modeling. These parameters are related to the pole parameters using Eq. 2.33. The resulting dielectric function is shown in Fig. 2.3 together with the reference measurement data. Although the fitting is good in general, focus has been put on the frequency range around 60 GHz where the expected bandwidth of antennas is located. The obtained poles form the basis for the relation between the electric polarization and the electric field as given by Eq. 2.34 [33].

Table 2.1: Parameters of a two-pole Lorentz Model for Atmospheric Attenuation at Sea Level.

Pole	**a** $(rad/s)^2$	**b** $(rad/s)^2$	**c** (rad/s)	**d**
1	$1.7367\text{x}10^{16}$	$1.4063\text{x}10^{23}$	$3.6\text{x}10^{10}$	1.0
2	$3.1545\text{x}10^{15}$	$1.5093\text{x}10^{23}$	$2.0\text{x}10^{10}$	1.0

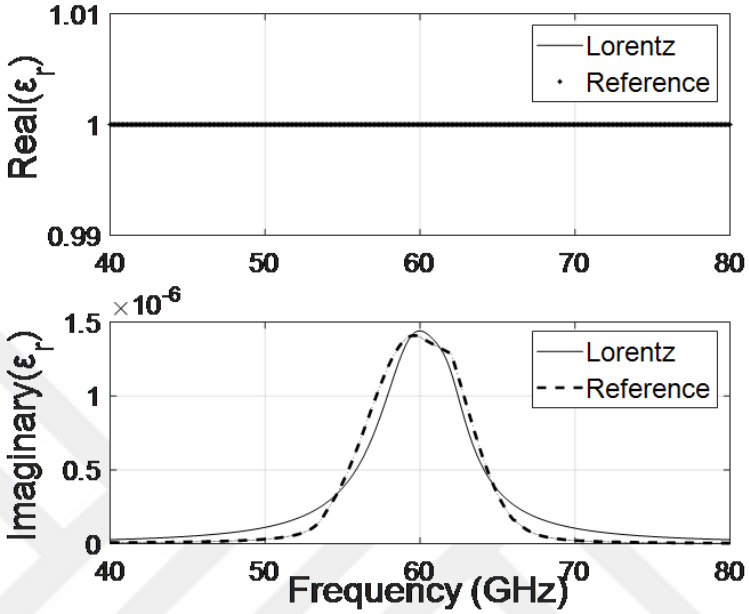

Figure 2.3: Real and imaginary parts of the dielectric constant function of the atmosphere as obtained from the empirical attenuation function ([19], dashed line) and the corresponding 2-pole Lorentz fit (solid line) for sea level conditions.

2.3.4 A Three-pole Lorentz Model for the Atmosphere at 60 GHz

Adding more poles gives more accuracy to the fitting process. However, the computational cost also increases. It was found that with three poles, the accuracy of the model increases without adding too much burden on the computations. This section shows the model results with three poles used in the Lorentz equation. Table 2.2 shows the values of the a, b, c and d model parameters for a 3-pole Lorentz function. The resulting dielectric function is shown in Fig. 2.4 together with the reference measurement data [32].

Table 2.2: Parameters of a three-pole Lorentz Model for Atmospheric Attenuation at Sea Level.

Pole	**a** $(rad/s)^2$	**b** $(rad/s)^2$	**c** (rad/s)	**d**
1	2.0245x10^{16}	1.5210x10^{23}	3.0x10^{10}	1.0
2	2.4546x10^{15}	1.3690x10^{23}	3.2x10^{10}	1.0
3	2.7960x10^{15}	1.2709x10^{23}	1.2x10^{10}	1.0

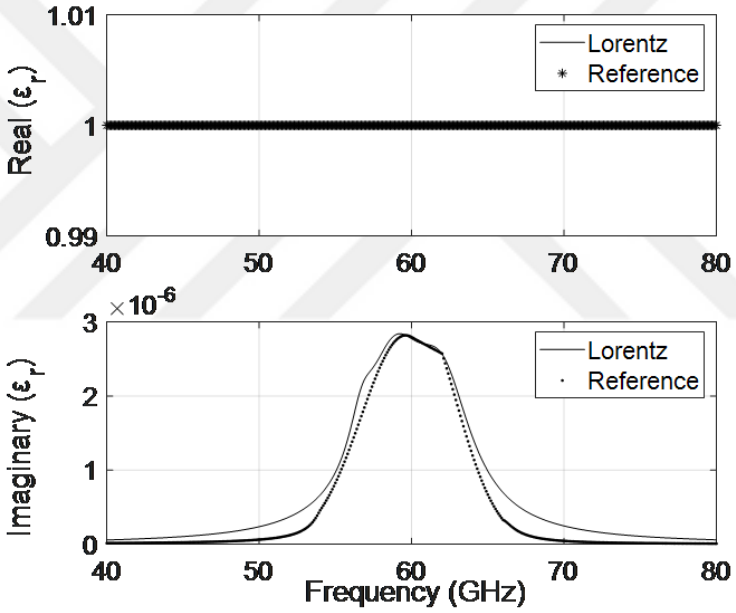

Figure 2.4: Real and imaginary dielectric constant curves of the atmosphere as obtained from the empirical attenuation function ([19], dashed line) and the corresponding 3-pole Lorentz fit (solid line) for sea level conditions.

2.4 The FDTD Algorithm

Next, the frequency-domain dielectric function is incorporated in a time-domain simulator using the ADE-FDTD method. Eqs. 2.28 and 2.34 can be given in the time domain utilizing the Inverse Fourier Transform, as reported in [31]. The procedure results in a second order differential equation for the electric polarization

vector given by

$$bP + c\frac{d}{dt}P + d\frac{d^2}{dt^2}P = a\varepsilon_0 E \tag{2.40}$$

Using finite-difference approximations, the time domain update equation for the linear polarization in Eq. 2.40 becomes

$$b\frac{P^{n+1} - P^{n-1}}{2} + c\frac{P^{n+1} - P^{n-1}}{2\Delta t} + d\frac{P^{n+1} - 2P^n + P^{n-1}}{2\Delta t^2} = a\varepsilon_0 E^n \tag{2.41}$$

$$P^{n+1} = C_1 P^n + C_2 P^{n-1} + C_3 E^n \tag{2.42}$$

The constants in Eq. 2.42 are given by

$$C_1 = \frac{4d}{2d + c\Delta t + b\Delta t^2} \tag{2.43}$$

$$C_2 = \frac{-2d + c\Delta t - b\Delta t^2}{2d + c\Delta t + b\Delta t^2} \tag{2.44}$$

$$C_3 = \frac{2a\varepsilon_0 \Delta t^2}{2d + c\Delta t + b\Delta t^2} \tag{2.45}$$

where n is the time index and Δt is the time step. All field components and parameters are arranged on the FDTD computational grid using the standard Yee's cell. The time-domain algorithm proceeds as follows. First, the electric flux densities are evaluated using Maxwell's curl Eq. 2.21 with available magnetic field samples.

$$D^{n+1} = D^n + (\nabla \times \mathbf{H})^{n+\frac{1}{2}} \tag{2.46}$$

Next, the linear polarization vector is updated using Eq. 2.42. Third, the electric field intensity components are updated using the time-domain version of Eq. 2.27 as

$$E^{n+1} = \frac{D^{n+1} - \sum_a^M P^{n+1}}{\varepsilon_0 \varepsilon_\infty} \tag{2.47}$$

Finally, the second Maxwell's curl Eq. 2.22 is used to calculate the magnetic field components.

$$H^{n+\frac{3}{2}} = H^{n+\frac{1}{2}} - \frac{1}{\mu}(\nabla \times \mathbf{E})^n \tag{2.48}$$

The flowchart in Fig. 2.5 describes the sequence of calculations in the resulting algorithm.

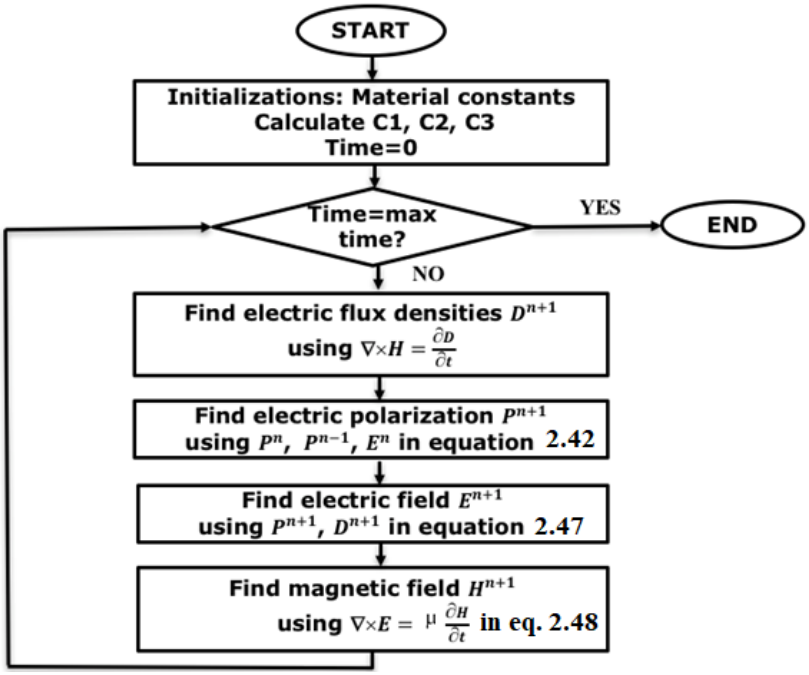

Figure 2.5: Flowchart of the calculation sequence in the time-domain algorithm.

2.5 Simulations and Results

To test wave propagation using the proposed atmosphere model, the FDTD simulation algorithm presented earlier is implemented. A time-limited pulse of a Gaussian form given by

$$A(t) = A_0 e^{-[\frac{t-t_0}{t_p}]^2} cos[\omega_c(t-t_0)] \tag{2.49}$$

is used as the antenna output, where A_o is the initial pulse amplitude, t is time variable, t_o is the offset time, t_p is the pulse waist and ω_c is the central frequency. The parameter t_p is used to steer the frequency contents of the pulse. In this work, a pulse waist of 20 picoseconds is used such that it covers a large frequency

band around 60 GHz, which is taken as the central frequency. A plane wave propagation in a one-dimensional sea-level atmosphere of initial amplitude 1 V/m is considered. The value of the spatial step is set to a very small fraction of the smallest wavelength involved in propagation. This is required to ensure that numerical dispersion is significantly minimized, and that channel dispersion is correctly represented. Accordingly, a spatial step size of 0.01 mm was used. The stability of the algorithm is determined by the standard Courant-Friedrichs-Lewy condition for the FDTD method, which is given by [34].

$$\Delta t \leq \frac{1}{\upsilon_{max}\sqrt{(\frac{1}{\Delta x^2})+(\frac{1}{\Delta y^2})+(\frac{1}{\Delta z^2})}} \tag{2.50}$$

A time step of 0.03 ps satisfies this condition. Numerical dispersion is an artifact of the approximation of the spatial derivatives in finite differences. Because the spatial step is finite, errors in data transmission throughout the computational grid propagate and accumulate. The general guideline is to make the spatial step a very small fraction of the smallest wavelength involved in the propagation. This problem becomes more serious if the medium of propagation is itself dispersive. Consequently, with high levels of space resolution, the memory requirement for the simulation of hundreds of meters of propagation distance becomes unaffordable. To solve this problem, the rotating boundary conditions have been used.

2.5.1 The Rotating Boundary Conditions

The basic concept of this technique is to tie the ends of the computational domain in the propagation directions such that the propagating wave moves in what resembles a circle. In this case, the computational domain appears infinite in the propagation direction. As shown in Fig. 2.6, the pulse propagates across the whole domain, exits the computational window from one boundary and re-enters from the other boundary to start propagating the domain again. The rotating boundary conditions are thus defined as follows. For the first Maxwell's equation,

the curl is evaluated in one-dimensional case using,

$$\frac{\partial D}{\partial t} \mid_{i=i_1} = (H_{i_1} - H_{i_{max-1}})/\Delta x \tag{2.51}$$

and

$$\frac{\partial D}{\partial t} \mid_{i=i_{max}} = (H_{i_{max-1}} - H_{i_1})/\Delta x \tag{2.52}$$

In equations 2.51 and 2.52, i_1 and i_{max} are the first and last points in the computational domain, and Δx is the spatial step. The curl in the second Maxwell's equation is treated similarly.

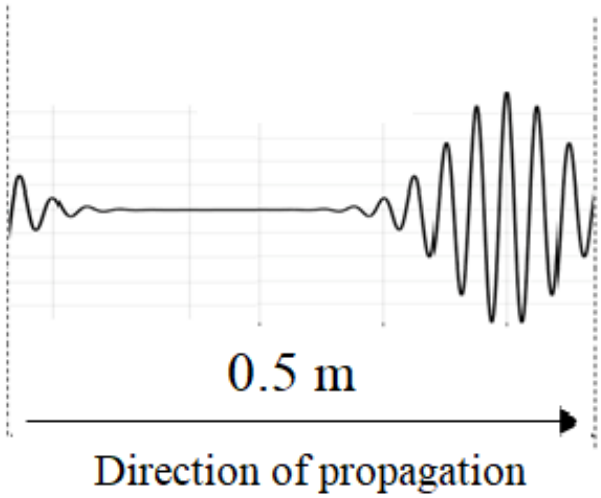

Figure 2.6: Pulse propagation in rotating boundary conditions. The total length of the computational window is half a meter.

The initial size of the computational domain is set to half a meter. The choice of this initial domain size ensures that it is wide enough to comfortably accommodate the pulse at any time throughout the simulation, even with the resulting dispersion due to the channel. The pulse trans passes the computational domain for multiples of times to achieve a certain propagation distance. In this study, the pulse is propagated well over one kilometer. Also, a reference simulation in a lossless atmosphere was carried out such that comparisons are possible.

2.5.2 Analysis of Propagation Results

In this study, the pulse is propagated well over one kilometer. Also, a reference simulation in a lossless atmosphere was carried out such that comparisons are possible. Fig. 2.7 shows snapshots of the time-domain electric field waveform at different distances. The figure clearly demonstrates the change in both amplitude and phase of the original pulse as it propagates in the atmosphere. The time scale of the snapshots has been adjusted between 0 - 7000 of time steps. In particular, Fig. 2.8 shows the time profile of the propagating pulse at 1000 meters as compared with the reference waveform for a lossless atmosphere. The attenuation and dispersion of the pulse is evident.

To validate the numerical model, power calculations have been performed. The spectrum of the received signal power after propagating 1000 m has been produced. At any given location, the power density is given by

$$\mathbf{S} = \frac{1}{2}\mathbf{E} \times \mathbf{H}^* \tag{2.53}$$

For a wave propagating along the x direction, the real power density is given by

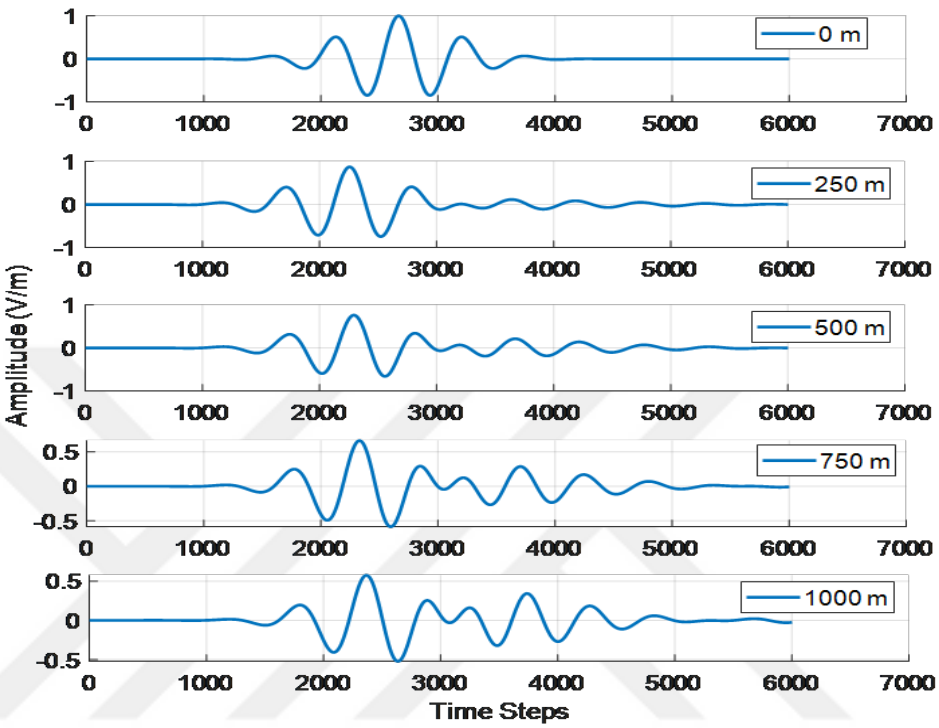

Figure 2.7: Time profile of the received electric fields at distance of 0, 250, 500, 750 and 1000 meters, with attenuation.

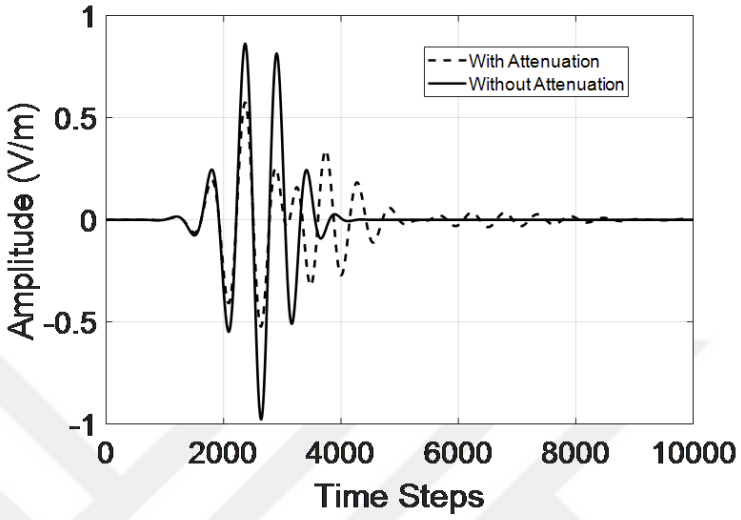

Figure 2.8: Time profile of the received electric field at distance of 1000 meters, with and without attenuation.

$$S(f)_{x,r} = \frac{1}{2}[E(f)_{y,r}H(f)_{z,r} + E(f)_{y,i}H(f)_{z,i}] \tag{2.54}$$

where the subscripts r and i denote the real and imaginary parts, respectively. The time samples for the electric field and magnetic field are collected, then using the Discrete Fourier Transform the values of electric and magnetic fields are found in frequency. Lastly power is calculated by utilizing the Eq. 2.54.

The amount of received power at several distances for the lossless and lossy atmosphere are shown in Fig. 2.9 and Fig. 2.10, respectively. It is clearly seen from the figure that a signal at 60 GHz loses more than 97% of its initial power within the first kilometer. The propagation of the 50, 60 and 70 GHz frequency components are shown separately in Fig. 2.11, where normalization has been made to the input value for each frequency component. Table 2.3 and Fig. 2.12 show the comparison between the amount of loss per kilometer, as given by the reference attenuation curve in Fig. 2.2 and by the FDTD simulation, for selected frequencies. The slight discrepancies in the power loss are attributed to the imperfections in the fitting process.

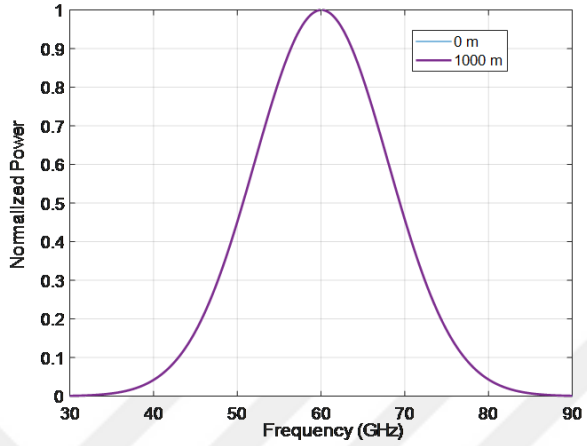

Figure 2.9: Normalized signal power at different propagation distances versus frequency for a lossless atmosphere.

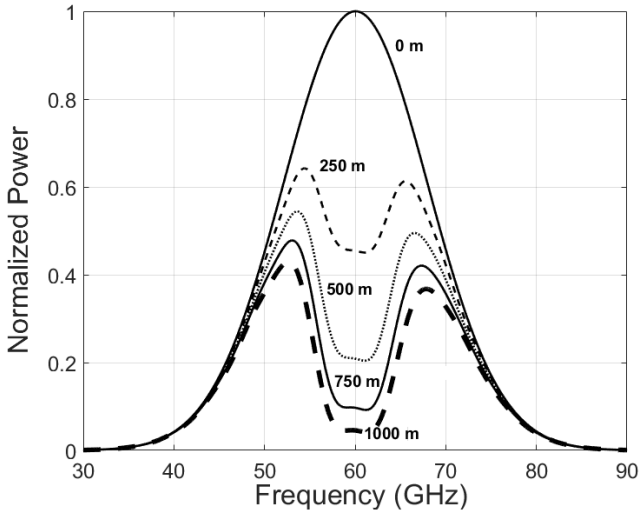

Figure 2.10: Normalized signal power at different propagation distances versus frequency for a lossy atmosphere.

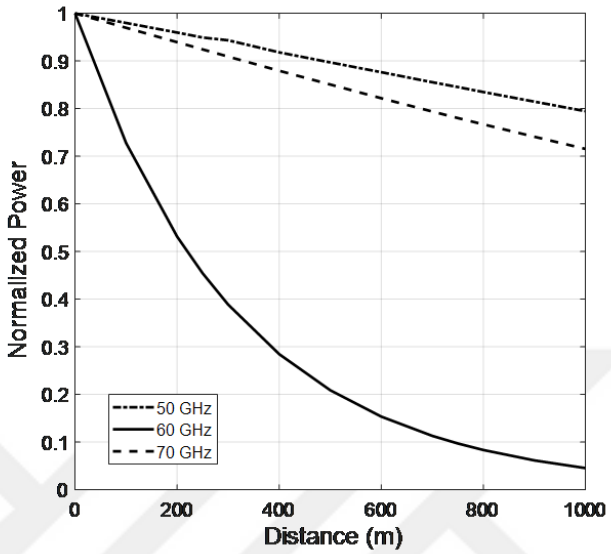

Figure 2.11: Normalized received power for the 50, 60 and 70 GHz frequency components versus propagation distance.

Table 2.3: Loss comparison between simulation results and reference data.

Frequency	**Loss(dB/km)**	
(GHz)	***Reference***	***Simulation***
57	8.78	9.00
58	11.43	11.42
59	15.23	14.26
60	15.26	16.04
61	14.89	14.61
62	14.51	11.93
63	10.75	9.61

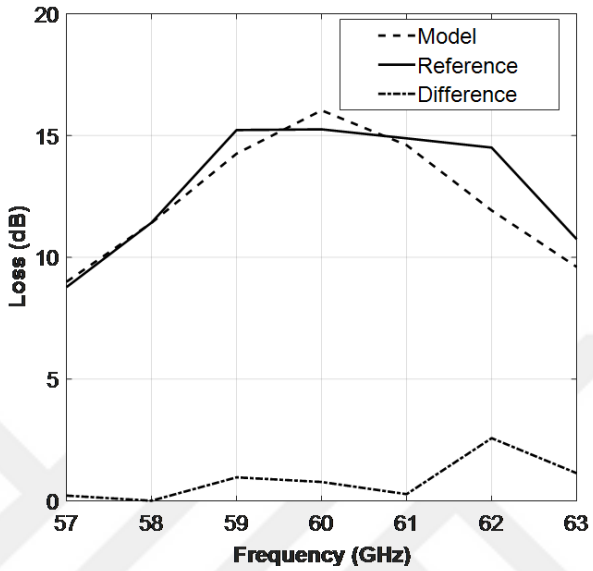

Figure 2.12: Estimated loss after propagation of 1000 meters, as given by the simulation model. The reference values and the difference are shown for comparison.

2.6 Conclusions

A propagation model for atmospheric absorption of 60 GHz band signals has been developed. The model is incorporated in an FDTD numerical simulator as a multi-pole material dispersion term using the ADE technique. The rotating boundary conditions have been used to allow for long propagation distances. Also, the validity of the model has been demonstrated. This model is very useful in the study of many situations involving free space communications with the possibility of incorporating different scenarios, such as reflections from buildings, presence of ground, terrain and water bodies and interference. It can be added to commercial electromagnetic software packages as a separate material module. The results are also useful in the prediction of propagation power loss such that methods for loss compensation can be devised. In the light of the obtained results, it is shown that one such method increase the directivity value of the basic antenna. This subject is covered in the proceeding chapters.

Chapter 3

DIELECTRIC FABRY-PEROT RESONATOR ANTENNAS

Directive antennas play a critical role to overcome the difficulties in most radar, satellite and 5G applications. Conventionally, high directivity requirements in antenna applications are met by utilizing antenna arrays, reflectors and lens antennas. The Fabry-Perot Resonator (FPR) antennas have been included in antenna applications in order to improve directivity performance and conformal deployment capability [35, 36, 37, 38, 39]. FPR antennas have the potential to be a good alternative to classical high directional antennas, with the advantages of low cost, structural simplicity, and ease of fabrication. In this part of the thesis the effect of dielectric slabs on the antenna directivity improvement in a certain direction is investigated by utilizing the FPR antenna concept. Investigation of the directivity by utilizing the FPR antenna concept are carried out. In this chapter, a brief theoretical background is given. Also, a number of recent studies and a review of the literature in this field are presented.

3.1 The Theory of the Fabry-Perot Resonator

Fundamentals of the Fabry-Perot Resonator (FPR) theory were laid originally during optical studies [40] . Its operating principle is based on multiple wave reflections between reflecting plates which are closely placed. This theory can also be used in FPR antennas [41]. An electrical resonator allows oscillations at resonant frequency and it stores energy at that frequency. An FPR resonator stores energy or filters the light at the resonant frequency. Consider two metallic mirrors M_1 and M_2 which are standing opposite to each other and are well-aligned, with free space between them, as shown in Fig. 3.1(a). The reflection of light between the mirrors (in the cavity) leads constructive and destructive interferences. The waves traveling from M_1 interfere with the waves reflected from M_2. That leads to a series of standing or stationary EM waves as shown in Fig. 3.1(b).

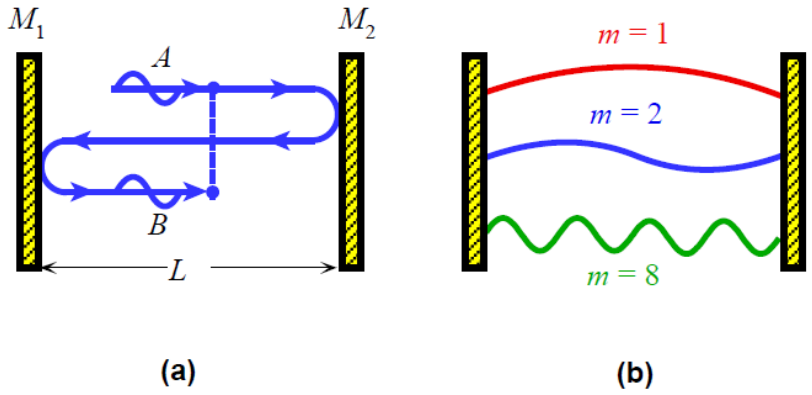

Figure 3.1: (a) The reflection between two flat mirrors (b) The integer number of half wavelengths that can fit into the cavity [42].

Since the electric fields must be zero at the mirrors, only an integer number m of half wavelengths $\lambda/2$ can fit into the cavity length L, such that

$$m(\frac{\lambda}{2}) = L, \qquad m = 1, 2, 3, ... \tag{3.1}$$

This formulation defines the cavity modes and each particular allowed wavelength, that is labeled as λ_m, satisfies this equation for a given m value. Each value of

m defines a cavity mode as shown in Fig. 3.1(b). Since the frequency f and wavelength λ are related by $f = \nu/\lambda$, the corresponding frequencies of these modes, f_m, are the resonant frequencies of the cavity and are given by

$$f_m = m(\frac{\upsilon}{2L}) = mf_0, \qquad f_0 = \frac{\nu}{2L} \tag{3.2}$$

where f_o is the lowest frequency corresponding to fundamental mode, $m = 1$, and v is the speed of light in the cavity medium, given by $c/\sqrt{\varepsilon_r}$. The separation of any two neighboring modes $\Delta f_m = f_{m+1} - f_m = f_0$ is called the "free spectral range" (FSR).

The intensity of the cavity modes can be obtained using the following analysis, which follows [42]. Consider an arbitrary wave such as A traveling towards the right at some instant, as shown in Fig. 3.1(a). After travelling one round trip this wave will be traveling towards the right again but as wave B. However, due to mirror reflections, wave B will have a different amplitude and phase than wave A. If the mirrors are identical with reflection coefficient of magnitude r, wave B will accumulate one round trip phase difference of $k(2L)$ and a magnitude factor of r^2 with respect to wave A, where k is the phase constant. When the waves A and B meet, the result of interference is

$$A + B = A + Ar^2e^{-j2kL} \tag{3.3}$$

This process will continue for many rounds, and after infinite round-trip reflections the resultant electric field inside the cavity E_{cavity} can be written as

$$E_{cavity} = A + B + ... = A + Ar^2e^{-j2kL} + Ar^4e^{-j4kL} + Ar^6e^{-j6kL} + .. \tag{3.4}$$

The closed-form expression for the summation of this geometric series is given by

$$E_{cavity} = \frac{A}{1 - r^2e^{-j2kL}} \tag{3.5}$$

From the field of the cavity we can calculate the intensity as

$$I_{cavity} = |E_{cavity}|^2 \tag{3.6}$$

Further, for simplicity of the expression we can use reflectance $R = r^2$. Then, the intensity can be now written as

$$I_{cavity} = \frac{I_0}{(1-R)^2 + 4Rsin^2(kL)} \tag{3.7}$$

where, $I_0 = A^2$ is the original intensity. The maximum intensity is obtained whenever $sin^2(kL)$ in the denominator of Eq. 3.7 is zero, which occurs with $kL = m\pi$. For this value, the maximum intensity becomes

$$I_{max} = \frac{I_0}{(1-R)^2}, k_m L = m\pi \tag{3.8}$$

Eq. 3.8 shows that radiation intensity distribution in the cavity is affected by the radiation loss of the cavity. In other words, a larger reflectance R means lower radiation intensity inside the cavity. The radiation loss increases as the reflectance decreases which means smaller reflectance causes more radiation loss.

Fig. 3.2 illustrates schematically the relative radiation intensity of the allowed modes as a function of frequency for frequencies around 60 GHz in an air-filled FP cavity with L=2.5 mm. The curves in the figure represent different mirror reflectance values: R = 0.4, 0.6 and 0.8. Each curve has been normalized to the maximum intensity. As indicated by Eq. 3.2, the intensity lines in the figure exhibit maxima at the resonance frequencies. Also, due to imperfect reflecting mirrors, the curves exhibit finite "line widths". If the mirrors are not perfectly reflecting, some radiation escapes from the cavity and the peaks become less sharp.

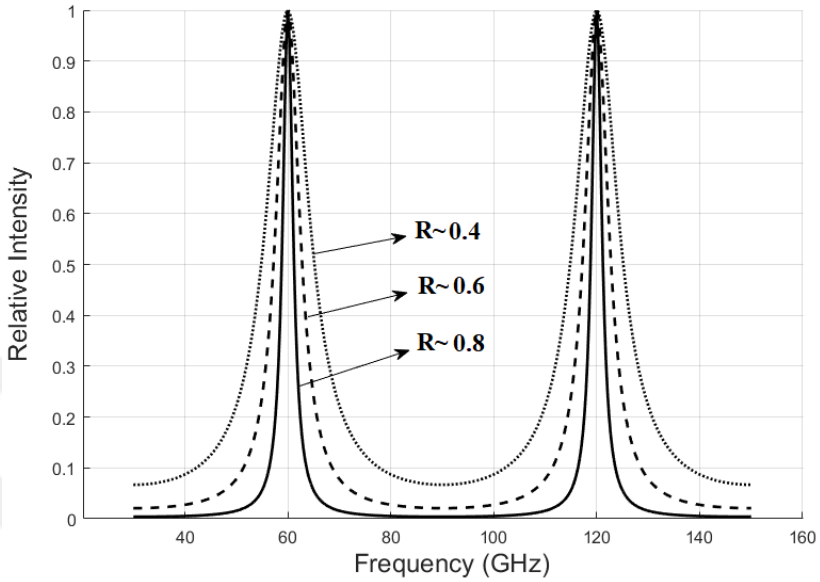

Figure 3.2: Relative radiation intensity inside the cavity vs frequency for various mirror loss values.

From Fig. 3.2 it is shown that the broader mode peaks belong to smaller R values and they have smaller distance between their maximum and minimum intensity values. The line width (sometimes called the spectral width) of the Fabry-Perot cavity is given by

$$\delta f_m = \frac{f_0}{F}; F = \frac{\pi R^{1/2}}{1-R} \tag{3.9}$$

F is called the finesse of the resonator. As R increases, the losses decrease and the finesse increases.

As a specific example, consider an air-filled FP cavity with dielectric walls made of a material with $\varepsilon_r = 11.7$ and cavity length of 2.5 mm. The fundamental mode (m=1) will have a frequency given by Eq. 3.2 at 60 GHz. The free spectral range $\Delta f_m = 60$ GHz. The mirror reflectance will be given by the air-cavity wall reflection coefficient and will equal to R=0.3. In this case, the maximum intensity inside the cavity is $I_{max} = 2.04 I_o$. The finesse of this cavity is $F = 2.46$, giving a line width of $\delta f_m = 24.4$ GHz. From this example, it is clear that a low intensity value and a large line width are obtained using a dielectric material for

cavity mirrors. The reasons that make dielectric mirrors preferable over metallic mirrors in antenna design are as follows. First, large quality factor of metallic cavities reduces the radiation bandwidth. Second, the metallic mirrors can produce resonances of their own, altering the overall radiation spectrum. Finally, the presence of the metallic cavity in the environment of the patch antenna introduces parasitic effects, again changing the radiation behavior of the antenna.

3.2 Application of the Fabry-Perot Technique in Antenna Design: A Literature Review

The Fabry-Perot structure has been utilized in the design of many radiating elements as early as 1956 [43], where the design consisted of a waveguide aperture and a partially reflecting screen (PRS) placed at half a wavelength from the ground plane. By replacing the PRS with a dense quarter wavelength dielectric sheet, a gain enhancement was reported [44, 45]. Later, an FPR antenna with several layers of dielectric sheets was proposed in 1993 [46]. Essentially the FPR antenna can be considered as a kind of electromagnetic bandgap (EBG) resonator antenna [47, 48, 49, 38, 50].

For the sake of this thesis, the literature review for this subject is divided into two parts in which they are mainly different in their operating frequency bands. Since the focus of this thesis is 60 GHz frequency band, works at 60 GHz frequency band will be considered first.

One of the earliest applications of the Fabry-Perot structure in the 60 GHz frequency band was reported in 1997 [51]. The work aimed at introducing phase shift in a Gaussian beam antenna (GBA). For this purpose, pairs of partially transparent mirrors on parallel fused quartz substrates were used and a controllable phase difference was obtained. A plane-parallel FP cavity was analyzed with the transmission line (TL) matrix theory and technique [52]. Two metal mesh mirrors performed cavities. The cavities are excited by a normally incident

plane wave. Although the TL matrix method and FDTD methods both had good agreement in resonant frequency, the TL method was rather inaccurate in bandwidth estimation [52].

A study which presents a beam shaping technique for the 60 GHz band was presented in 2003 [53]. A plane-parallel Fabry-Perot resonator including two uniform and non-uniform metal meshes excited by a horn antenna and a half-wavelength dipole antenna was used as a focusing device. The design resulted with radiation patterns that have very low side lobes. The directivity of the antenna was altered by adjusting value of the synthesized radius of curvature of the mirrors. Another study which enabled a significant increase in the directivity of a primary radiator was reported in [54]. A non-uniform metal mesh was used as output "reflecting mirror" of a plane-parallel FP resonator. This directivity study which used the FPR in the V-band gave a special attention to the 60 GHz frequency. The reflecting mirrors were made of metal strip gratings and the dimensions of the non-periodic output mirrors were much smaller than the working wavelength. It resulted with symmetric radiation patterns which have low side lobe levels. The directivity at 60 GHz was verified between 15 dB and 23.5 dB by synthesizing the radius of the curvature of the antenna.

A theoretical and an experimental study that deals with focusing of the FPRs is presented in [55]. The proposed antenna consists of plano-convex FP cavities, and horn-fed Gaussian beam antennas (Hf-GBAs) are used for excitation. Very good efficiency (40%-70%) obtained with also ultra-low side lobes (< -30 dB) that enables the effective reduction of multipath propagation. But at the same time Hf-GBAs are bulky and are not compatible with the integration of active circuits. Another study for the directivity enhancement was done using a plano-convex FP cavity [56]. The cavity was excited by a printed GBA through a dielectric coupling region called the printed fed-GBA (Pf-GBA). The directivity results of two antennas, fed by the same microstrip patch antenna array, lied between 15.5 dB and 23.5 dB and the efficiency was between 20% and 65%. A FPC antenna fed by an aperture in the ground plane at 60 GHz was proposed in 2009 [57]. The ground plane of the design was covered by a frequency selective surface (FSS). A gain value of 20 dB for the FPC antenna was achieved using a

single feed. The large conduction loss at millimeter wave frequencies and the way of mounting the PRS layer over the ground plane are important considerations in forming a FP cavity. Hereby periodic slots are used instead of periodic patches. A quartz substrate coated by a thin layer of gold and a slot with $1mm \times 0.24mm$ dimensions were used to design FPC antenna in [58]. Maximum gain of 17 dB is achieved and the antenna is operated at 42.8 GHz frequency.

Another study to increase the gain of a FP cavity antenna is proposed in [59], where a single-feed planar FP cavity antenna fed by a "coplanar waveguide (CPW-fed) slot dipole" designed for 60 GHz wireless systems was designed. The cavity is formed by utilizing a dielectric slab coated on both sides with thin layers of copper. One side of dielectric slab forms is used as the FSS layer and the other side provides the ground plane. Maximum gain of the antenna at 59.5 GHz is measured approximately 16.5 dB. In other gain enhancement study, a FP cavity antenna is designed by using a four-element sparse array of slot antenna [60]. It was shown that a larger GBW can be achieved by reducing the reflectivity of the FSS and by using a sparse array that feeds the cavity. A cavity is formed with a metallic FSS on top of a ground plane. The ground plane of FP cavity antenna is etched in order to feed the antenna by utilizing a slot antenna. The sparse array element is designed to operate at resonance frequency of the cavity. The inter-element spacing should be in the order of $0.5\lambda_0$, where λ_0 is the free space wavelength, to avoid formation of grating lobes. The suitable wavelength was suggested to be bigger than $0.5\lambda_0$ to decrease coupling between the array elements and to have the possible grating lobes suppressed to reasonable side lobe levels. The sparse-array provided more than 12.7 dBi gain from 58.17 to 61.70 GHz, and it was shown that the designed structure has almost the same gain-bandwidth value (GBW) with the single-fed structure, which is around 3.5 GHz.

A circularly polarized FPR antenna was reported in [61]. Results show a maximum gain of 16 dB at 60 GHz. The previous work was later transformed to another concept by changing the air-filled cavity to a dielectric slab [62]. The cavity is made of a single dielectric slab. When compared with the designs in [56, 57] and [63, 64], a single-layer FPC provides ease of fabrication and the number of

components added to the antenna structure decreases. Furthermore, it enables for the same substrate to place other components on it. The measurements showed a maximum gain of approximately 16 dB at 59.45 GHz (close to the resonance frequency of the cavity at 59.5 GHz) whereas the analytical measurements based on the transmission line (TL) model was 16.7 dB and the simulated full wave result was 17.15 dB. The 3-dB gain-bandwidth (GBW) of the measurement is 1.2 GHz and of the simulated one is 1.4 GHz.

Another study for the enhancement of the antenna directivity is proposed in [65]. A perforated metallic cap placed to form an FSS over a printed circuit board (PCB) was used. Accordingly, some other studies were performed by changing the perforated metallic FSS size and shape by using different substrate thicknesses. Moreover, the sensitivity of the antenna was investigated for the small variations of the fabrication and assembly, and it was shown that minor changes in design have undergone significant changes in antenna response. The radiation performance of estimated results of the antenna (using TL model) was tested using full-wave simulation, and measurement results for achieving the simple and directed V-band antennas showed that maximum broadside realized gain of the antenna was around 11 dBi and 13 dBi. An improved FPR antenna study of the one in [65] used a finite PRS [66]. A thick dielectric slab which consisted of two thin metallic surfaces from top and bottom with ε_r=6.15 is used for the 19×19 unit-cells of PRS. The designed geometry has a PRS part and a ground plane. The medium between them was air, and the antenna was fed by using a half-wavelength slot in the ground plane. Maximum gain of about 19.3 dBi was achieved with 5.2 GHz gain-bandwidth.

In 2017 M. Y. Mi et. al studied the antenna parameters of a FP cavity antenna with a single and double superstrates [67]. The whole structure has three substrates Rogers 3210, Rogers 4450 and Rogers 4003 from bottom to the top, respectively. The first substrate has patch antenna on top and aperture 1 on the top copper surface. Under substrate 1 there were substrate 2 and substrate 3 standing evenly. To decrease the permittivity, substrate 2 and substrate 3 had multiple rows of air holes. An FR4 was used to bond the superstrates, and the air-filled cavity was formed by digging a square hole. It is found that the

two-dielectric superstrate has peak gain of 12.68 dB.

Another FP cavity antenna to improve the gain-bandwidth study was done by using an inset fed microstrip patch antenna [68]. The first substrate which is located to the bottom has patch antenna on top surface and ground plane on bottom surface while the top substrate has PRS unit cells standing mutually to the antenna direction, and the two substrates are bonded by plastic spacers with a distance "h" (the cavity length). For the length "h" there is an equation that has to be satisfied. A frequency domain solver simulator is used, and the antenna has an impedance bandwidth of 5.6 GHz, 3dB-GBW of 4.6 GHz and 16.4 dBi gain. Another type of FPR antenna for the 60 GHz frequency is designed in [69]. The FPR antenna is produced with the following steps; the design of a dual-layer with unit-cells of PRS, the design of the slot antenna, and lastly the design of the printed ridge-gap waveguide (PRGW) antenna. An antenna design utilizing a FP cavity and an EBG was reported in [69]. The combined design of 2-D finite array of the dual-layer PRS and the PRGW designs, which is called as FPC-PRGW antenna produced an impedance bandwidth of 18.4% from 55.4 to 66.6 GHz, and maximum gain of about 12.2 dB.

A wideband single layer FPC antenna with a radial variation of the cavity permittivity is discussed in [43] by taking the antenna in [62] as a reference. The permittivity of the cavity varies gradually from the center. The design has a dielectric slab of Rogers RT/Duroid 5880 covered on bottom with a ground plane including a feeding slot and a FSS on top which is formed by periodic slots. The FPR resonates at 59.5 GHz with 3.2 GHz gain-bandwidth value. A related study which used a substrate design where the relative permittivity is gradually reduced from center to the edges achieved 17.48 dB directivity at 63 GHz with a 3-dB directivity fractional bandwidth of 43% [70]. An FPR antenna with TL model is designed to increase the gain at 63 GHz in [57]. The design consists of a ground plane with an FSS as a PRS. The case enhanced for thin FSS and the effect of ohmic losses is considered. Results show a 20 dB gain, and a GBW of 1 GHz.

A wideband millimeter-wave printed FPR antenna operating at 60 GHz is

designed by using multiple feeding [71]. The antenna comprises of substrate integrated waveguide (SIW)-based feeding source, which was designed on two Rogers 5880 substrates. A quasi-curve reflector formed by four conductive rings with different diameters and a planar PRS made of Rogers 4360G2 are implemented. The quasi-curve reflector has multiple reflections of incident wave and that forms the FP cavity. While the antenna gain is 8 dBi when there is no PRS on top, the parametric studies of the introduced design showed the measured gain of 17.6 dBi and the measured directivity of 18.8 dB. A design based on a rectangular FP resonator intended for broadband WLAN applications is reported in [72]. The proposed design consists of a CPW feed line, a patch antenna, a DFPR and supporting dielectric-posts. The patch antenna is located on the substrate with the help of fixing posts. Similarly, the DFPR is also placed on the patch antenna by using fixing posts. The patch antenna and the DFPR are designed at 60 GHz operating frequency. The measurement results show that the antenna has a limited gain of 3.6 dBi, while the -10 dB bandwidth was 17.5 GHz.

Fabry-Perot-based antenna designs have also been reported in literature for frequencies outside the 60 GHz band. In the following, a brief review of the most prominent reports is given.

A Fabry-Perot antenna with a high directivity for Ku Band (12-18 GHz) is introduced in [73]. The antenna was of a parallelepipedal structure and it consisted of a cavity which is made of a copper ground plane and a single metallic (copper) grid. The ground plane shows a perfect mirror behavior while the copper grid acts a partially reflecting mirror. The excitation is provided by a square patch antenna that was placed above the ground plane. The bi-periodic array of the grid was made of 40×40 elementary cells. The cavity is filled by a foam having a permittivity of 1.07 at the operating frequency. High directivity values were observed at 15.6 and 14.8 GHz. A study of an antenna operating at 10 GHz by using Artificial Magnetic Conductor (AMC) PRS is introduced by Y. Sun et al. [74]. The proposed antenna is integrated into the grounded dielectric substrate by using PCB technique. The AMC was used as a partially reflecting screen and the achieved gain was about 12.5 dBi. Another study which focused on gain enhancement proposed a FPR antenna that uses a single superstrate [75].

The introduced design consists of a PEC ground plane and a single superstrate which has two adjacent dielectric slabs. There is a separation between the ground plane and the superstrate which is considered as free space. The achieved 3-dB gain-bandwidth is 12.6% and directivity is 15 dBi. The size of the superstrate is optimized and a bandwidth of 34.8% achieved with directivity of 15.7 dBi. In order to increase the gain-bandwidth value further, multi-layers were used [76]. Instead of the PRS with no-gap which is used in previous study, an air-gap consisting of hexagonal nylon spacers between two dielectrics is used to form the PRS. One of the dielectrics which has the bigger dielectric constant ($\varepsilon_r = 6.15$) is positioned between the ground plane and the upper dielectric layer ($\varepsilon_r = 2.2$). In addition, a slot-coupled patch antenna was used for feeding due to its low profile. The calculated and measured 3 dB gain-bandwidth is from 13.5 to 17.5 (25.8%) with a gain of 15 dBi. This design was improved further by using two complementary FSS layers [76]. The same feeding type of the previous study was used. One side of PRS consisted of square patches and the opposite surface consisted of square apertures. The maximum gain was found to be 13.8 dBi and the 3 dB gain-bandwidth obtained was from 8.6 to 17.5 GHz (25.8%).

The following chapter presents a new and different perspective to FPC antenna designs.

Chapter 4

DIELECTRIC FABRY-PEROT RESONATOR-BASED PATCH ANTENNA

Dielectric Fabry-Perot resonators (DFPRs) utilize dielectric reflectors to generate resonance inside the cavity. In connection with antennas, DFPRs are preferred for a number of reasons. First, metal reflectors exhibit strong parasitic effects, leading to unwanted degradation of radiation characteristics. Second, with metal cavity walls, the cavity will have very high-quality factor leading to a narrow radiation bandwidth. Finally, metallic FP cavities can produce additional radiation modes, and hence altering the radiation spectrum. In this chapter, the integration of a DFPR with a patch antenna operating at 60 GHz for directivity enhancement is presented. The reference basic patch antenna is designed and characterized first. Afterwards, the DFPR-based patch antenna design and analysis with different parametric studies are discussed. All simulations are performed using COMSOL Multiphysics RF Module.

4.1 The Reference Antenna

There are many ways to excite a patch antenna. Here, the inset-fed method is used for excitation. For the inset-fed the inset gap dimensions, which are called as "stub length" and "stub width", are very critical for the impedance matching. Fig. 4.1 shows an inset-fed rectangular microstrip patch antenna configuration that operates at 60 GHz is designed on a dielectric substrate with antenna length (L), antenna width (W), feed line and inset gap (demonstrated with stub length and stub width). Table 4.1 shows the dimensions of the antenna and the stub dimensions.

Table 4.1: Design parameters for the reference antenna at 60 GHz.

Parameter	**Value**
Substrate thickness	0.254 mm
Antenna width (W)	1.66 mm
Antenna length (L)	1.20 mm
Feed line width	0.59 mm
Feed line length	0.785 mm
Stub width	0.155 mm
Stub length	0.350 mm
Relative permittivity (ε_r)	3.38

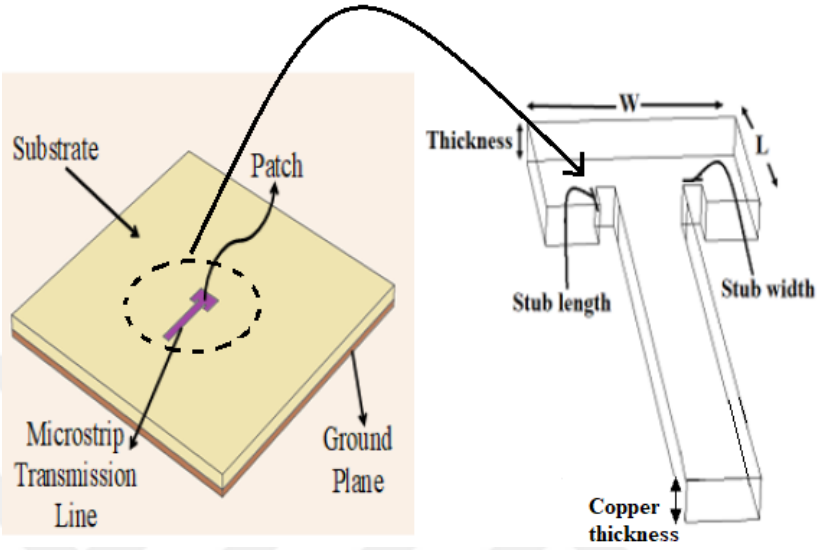

Figure 4.1: Rectangular patch antenna using inset feed method

The reference rectangular microstrip patch antenna dimensions are: the length of antenna is 1.20 mm, the width of antenna is 1.66 mm with the 2.77 mm $\times$ 2.77 mm substrate that has a dielectric constant of 3.38 and thickness of 0.254 mm.

In Fig. 4.2, the return loss graph of the rectangular microstrip antenna is shown. The y axis shows the return loss value in dB and the x axis shows the frequency in GHz. The return loss is around -43.184 dB at the resonance frequency of 60.37 GHz. At this frequency, the radiation pattern at $\phi = 0°$ is shown in Fig. 4.3. The pattern is typical of a standard patch antenna. The 3D far field of the reference antenna at resonance is shown in Fig. 4.4, whereas Fig.4.5 shows the electric field intensity over the patch. Electric field intensity showing the first mode characteristic of the wave on the antenna. The simulation shows a directivity at the maximum radiation direction of 7.16 dB on this antenna which is typical of a standard microstrip patch antenna performance.

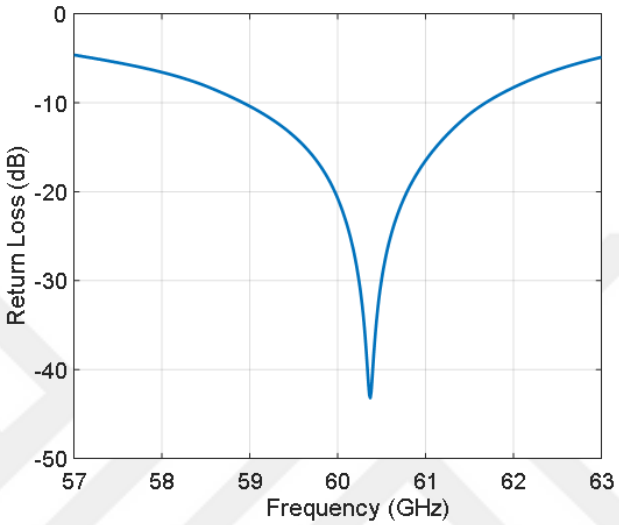

Figure 4.2: Return loss of the reference antenna.

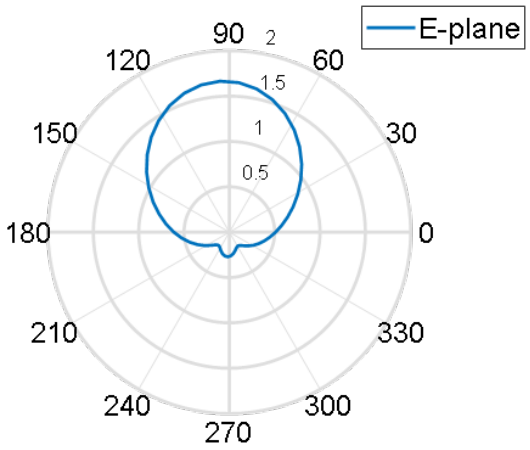

Figure 4.3: 2D E-plane radiation pattern of the reference antenna at resonance.

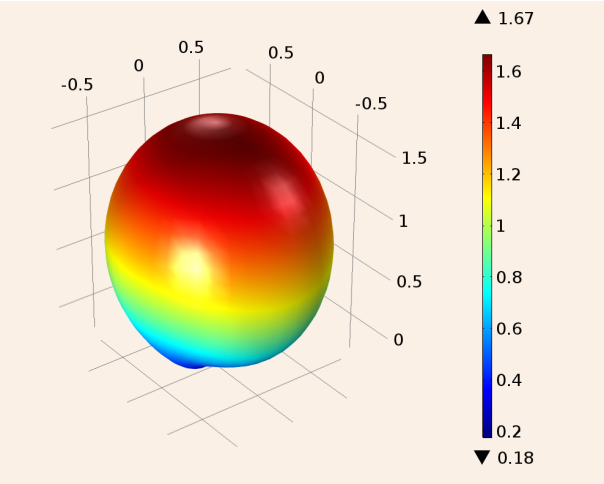

Figure 4.4: 3D radiation pattern of the reference antenna at resonance.

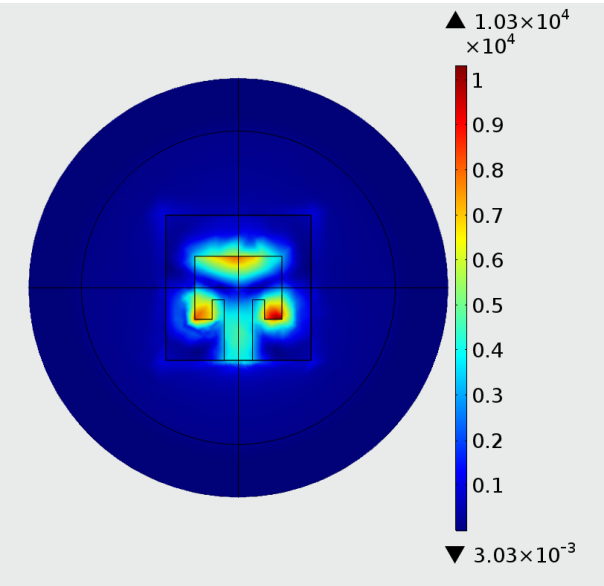

Figure 4.5: Electric field intensity of the reference antenna at resonance.

4.2 Dielectric Fabry-Perot Resonator Parametric Studies

In this section, parametric studies on the performance of the DFPR-based patch antenna are performed. As shown in Fig. 4.6, the DFPR is implemented on the top surface of the substrate, where the patch antenna is located. The patch antenna is thus located within the space of the DFPR cavity. Because the patch antenna is an edge radiator, the radiating edges are targeted by this cavity placement. The physical concept here is that the radiation modes of the patch antenna are coupled to the cavity modes. For the purpose of this thesis, the fundamental antenna mode is coupled to the fundamental mode of the DFPR structure ($m = 1$). This physical concept is similar to the coupling of optical modes in light-emitting devices to plasmonic modes [77], resulting in increased light directionality and extraction. This effect is sometimes referred to as the Purcell effect in photonics [77].

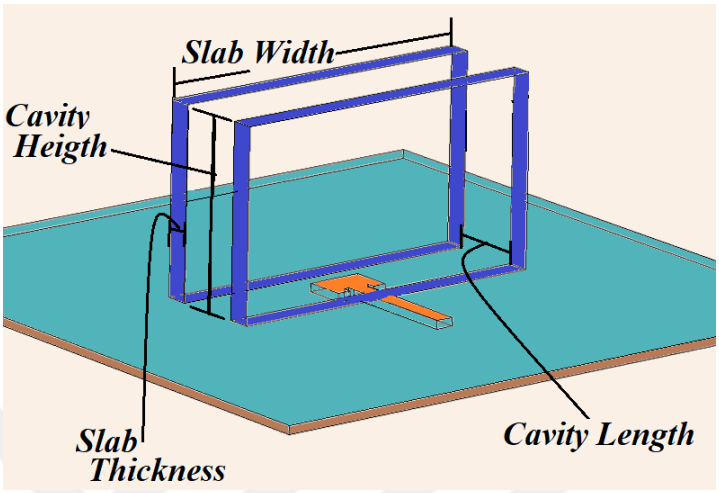

Figure 4.6: Schematic representation of the parametric studies of the DFPR antenna design.

The DFPR parameters include cavity length, cavity width, cavity height, slab thickness, slab array and filling material. The slab material is chosen such that it has a high contrast in dielectric constant with the cavity filling material to produce a high reflectance. The dielectric material used in all studies is silicon with dielectric constant of 11.7. For each study, antenna impedance matching is done to produce the best resonance conditions. Also, for each case, the antenna radiating characteristics, and in particular the directivity, are analyzed and gathered. The objectives of these studies are to validate the concept of directivity enhancement using the DFPR structure and second to come up with design guidelines for DFPR-based patch antennas.

The following subsections study, respectively, the cavity length, cavity width, cavity height, slab thickness, slab array and filling material of the DFPR based antenna.

4.2.1 Cavity Length

One of the most important parameters of any DFPR is the cavity length because it is directly tied to cavity resonance, as discussed in Chapter 3. The definition

of this parameter is shown in the top view of Fig. 4.7. In the following studies, the cavity length is varied starting from a small value that barely makes the cavity walls touch the antenna. Cavity width and height are set to 5 mm. The slab thickness is 0.7 mm. The filling material is air. Table 2.2 summaries the results of this parametric study. It is noticed that for a small cavity length the performance of the antenna is not favorable. However, as the length is increased, antenna directivity is improved. It appears that there is an optimal value for the cavity length that gives the best performance. This length value is naturally related to the cavity resonance condition. For 60 GHz resonance frequency, the corresponding wavelength is $\lambda_c = 5$ mm. If the FP cavity is filled with air, then the cavity fundamental mode resonance is $\lambda_c/2$ or 2.5 mm. The analysis of these results will be discussed in a following section.

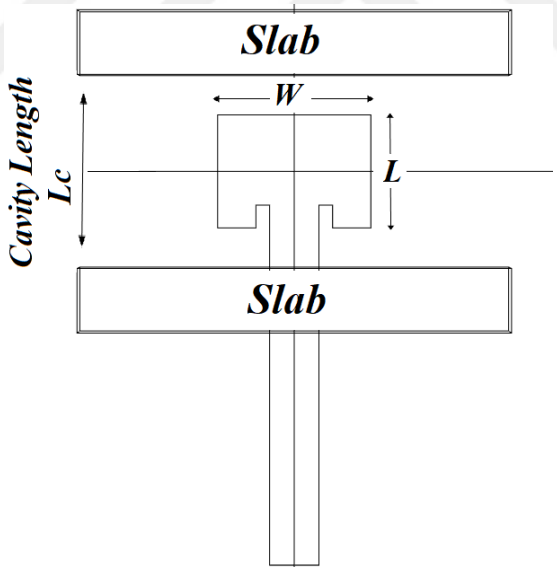

Figure 4.7: Geometry design of the DFPR antenna.

There are two important issues to be explained here. The first issue is related to the location of antenna resonance as given by the minimum of the return loss. Introducing the cavity in the surrounding environment of the antenna changes the effective dielectric constant of the substrate, and hence produces a shift in the resonance frequency.

Table 4.2: Simulation results of different cavity length studies of DFPR antenna.

Cavity/ Effective Length (mm)	**Return Loss (dB)**	**Resonance Frequency (GHz)**	**Directivity (dB)**	**Bandwidth (%)**
1.24/1.94	-19.077	59.00	8.3220	1.90
1.76/2.46	-17.00	59.50	13.409	6.89
1.80/2.50	-21.550	59.19	11.862	1.94
1.90/2.60	-16.371	60.30	13.052	7.46
2.1/2.80	-51.420	60.60	12.625	4.62
2.3/3.00	-48.103	59.30	12.265	4.38
2.5/3.20	-15.271	58.00	11.269	3.54

The second issue relates to the calculated effective length of the cavity. Because of the fact that the cavity walls are dielectric, the electromagnetic fields have a finite penetration inside the slabs. The effective cavity length is calculated by adding half of the slab thickness on both sides.

4.2.2 Cavity Width

The definition of the cavity width parameter is shown in the top view of Fig. 4.8. In this study, the cavity width is varied starting from a small value that makes the cavity walls enclose the antenna. Cavity length and height are set to 1.8 and 5 mm, respectively. The slab thickness is 0.7 mm. The filling material is air. Table 4.3 summaries the results of this parametric study.

The results show some variations in the antenna directivity with the cavity width. There exists an optimum value of cavity width around 5 mm. These results will be analyzed in a subsequent section.

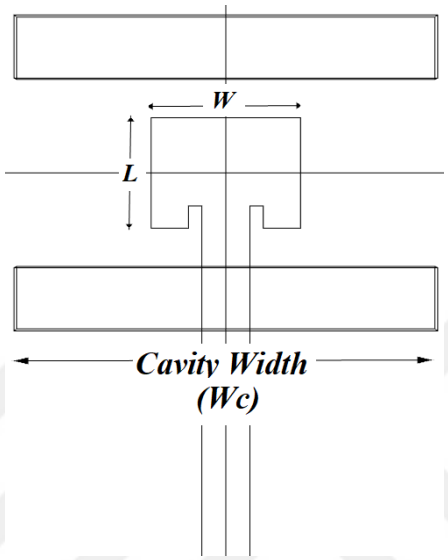

Figure 4.8: Top view of the DFPR antenna representing cavity width.

Table 4.3: Simulation results of different cavity width studies of DFPR antenna.

Cavity Width (mm)	**Return Loss (dB)**	**Resonance Frequency (GHz)**	**Directivity (dB)**	**Bandwidth (%)**
3	-23.372	60.1	8.9253	3.99
4	-25.034	61.0	11.831	4.26
5.75	-46.640	60.6	12.477	4.62
7	-24.972	61.3	11.539	4.08
10	-33.272	60.3	10.372	2.98

4.2.3 Cavity Heigth

The definition of the cavity height parameter is shown in Fig. 4.9. In this study, the cavity height is varied such that enhancement in directivity is studied. Cavity length and width are set to 1.8 and 5 mm, respectively. The slab thickness is 0.7 mm. The filling material is air. Table 4.4 summaries the results of this parametric study.

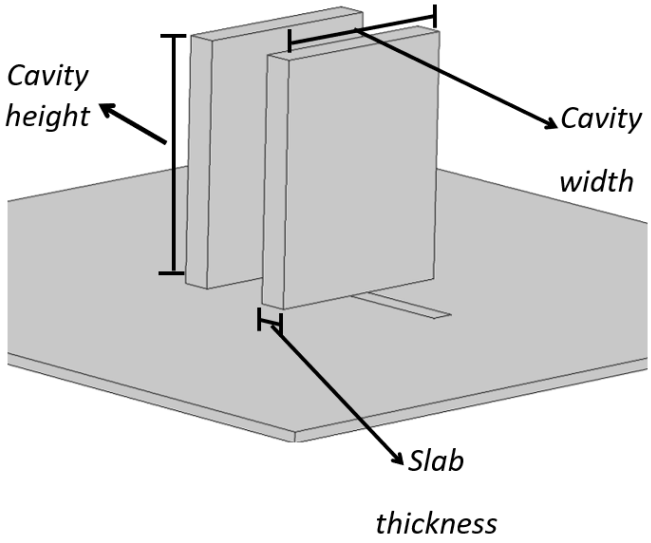

Figure 4.9: Prospective view of the DFPR antenna.

The results show some variations in the antenna directivity with the cavity height. There exists an optimum value around cavity height of 5 mm. These results will be analyzed in a subsequent section.

Table 4.4: Simulation results of different cavity height studies of DFPR antenna.

Cavity Height (mm)	**Return Loss (dB)**	**Resonance Frequency (GHz)**	**Directivity (dB)**	**Bandwidth (%)**
1.20	-28.148	60.60	9.3455	6.12
1.68	-23.773	59.90	9.2628	5.98
3.00	-42.641	59.20	11.716	2.53
4.70	-54	60.50	11.583	6.08
6.00	-41.375	60.30	13.289	5.14
8.00	-18	59.70	11.548	5.92
10.0	-25.403	60.30	9.5021	6.00

4.2.4 Slab Thickness

Another parameter that affects the antenna performance and directivity is the slab thickness. This parameter is of particular importance because it is in the direction of the standing waves forming inside the cavity. The definition of the slab thickness parameter is shown in Fig. 4.9. In this study, the slab thickness is varied such that enhancement in directivity is studied. Values of the slab thickness are carefully chosen to include the resonance condition of the cavity formed within the slab itself. Cavity length, width and height are set to 1.8, 5 and 5 mm, respectively. The filling material is air. Table 4.5 summaries the results of this parametric study. The results show substantial variations in the antenna directivity with the slab thickness. As expected, the optimum thickness value corresponds to the resonance condition of the cavity effectuated between the slab walls and air. Inside the slabs, the resonance condition for the fundamental mode is given by $\lambda_s/2$, where λ_s is the wavelength inside the slab. This value is very close to 0.7 mm. These results will be analyzed in a subsequent section.

Table 4.5: Simulation results of different slab thickness studies of DFPR antenna.

Slab Thickness (mm)	**Return Loss (dB)**	**Resonance Frequency (GHz)**	**Directivity (dB)**	**Bandwidth (%)**
0.1	-35.604	60.40	8.4704	5.13
0.4	-24.256	61.20	9.8963	5.60
0.6	-31.407	60.90	11.157	3.28
0.7	-48.437	60.70	12.379	4.77
0.9	-18.369	59.10	9.6655	2.19

4.2.5 Slab Array

Additional parallel slabs can be added on either side of the cavity to improve the cavity performance and hence directivity. An array of slabs is shown in Fig. 4.10. In this study, the number of slabs on either side is varied such that enhancement in directivity is studied. Cavity length, width and height are set to 1.8, 5 and 5 mm, respectively. The slab thickness is 0.7 mm. All slabs are identical with spacing between them of 0.3 mm. The filling material is air. Table 4.6 summaries the results of this parametric study.

The results in the table show that adding more slabs in this case does not improve the directivity of the antenna. This is a reasonable result for two reasons. First, the slabs used are thick and hence field penetration is very limited. Second, the dielectric constant of the slabs is high such that field are confined within the first slab. To make the array technique effective, one needs to design a Bragg grating structure with slabs and spacing specified to implement a perfect dielectric mirror, which is beyond the scope of this thesis.

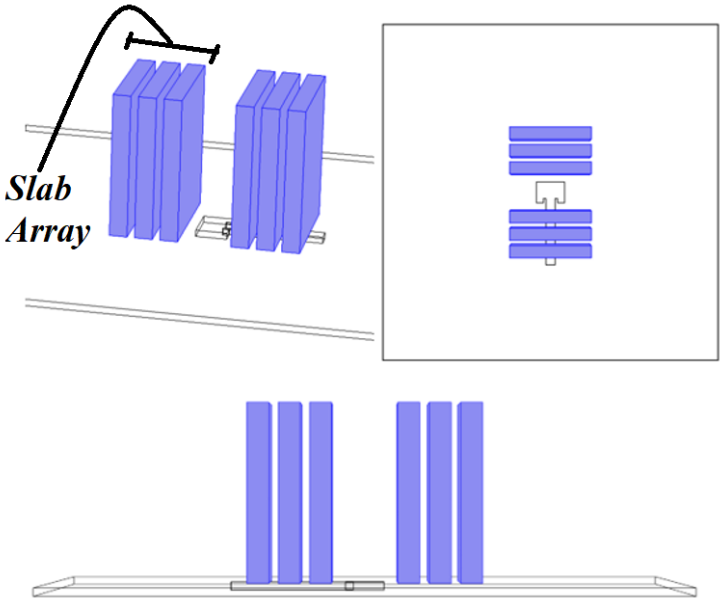

Figure 4.10: Slab array geometry design views with three different aspects.

Table 4.6: Simulation results of different slab array studies of DFPR antenna.

Array Number	**Return Loss (dB)**	**Resonance Frequency (GHz)**	**Directivity (dB)**	**Bandwidth (%)**
Single	-48.437	60.70	12.379	4.77
Double	-30.394	61.0	9.0489	4.09
Quadruple	-34.726	61.0	9.9334	5.40

4.3 Filling Material

The filling material inside and outside the DFPR has been so far taken as air. It is important to consider the effects of having different filling materials on the performance of the DFPR-based antenna. Filling material can be used as a way to protect the integrity of the slabs from accidental damage and make the

antenna structure more durable in real-life applications. It should be noted that the filling material dielectric constant should be as close to 1.0 as possible for two reasons. First, higher dielectric materials might produce a big shift in the cavity resonance. Second, the high contrast between the slabs dielectric constant and the filling material has to be maintained for better reflectance.

In the following subsections, the effect of the cavity filling material will be discussed first. Afterwards, the effect of a protective material that covers the whole upper surface of the substrate will be considered.

4.3.1 Cavity Filling Material

A dielectric material that has a lower dielectric constant than the slabs is used as a cavity filling, as shown in Fig. 4.11. Cavity length, width and height are set to 1.8, 5 and 5 mm, respectively. The slab thickness is 0.7 mm. Table 4.7 summaries the results of this study. Two filling materials are used, and the results are compared to the air filling case. One of the cases is for a real material (HPC 50 polymer foam, dielectric constant of 1.31) and one for a hypothetical material (dielectric constant of 1.5).

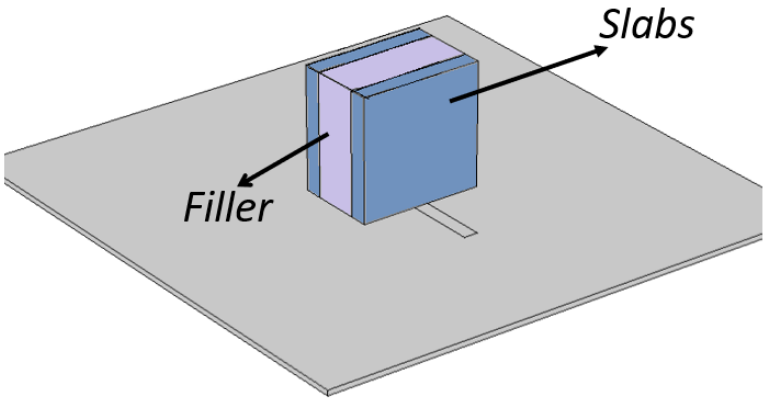

Figure 4.11: Geometry of the DFPR antenna with filling material.

The polymer foam material has a dielectric constant very close to one, so it is favorable. Also, this type of foam is widely used in industry in impact protection structures. The results in table 4.7 show that this filling does not cause significant effect on the directivity nor the resonance frequency of the patch antenna. So, the study shows it is possible to use this type of foam at 60 GHz reliably.

Table 4.7: Simulation results of filling material studies of DFPR antenna.

Material Dielectric Constant	**Return Loss (dB)**	**Resonance Frequency (GHz)**	**Directivity (dB)**	**Bandwidth (%)**
1.0	-46.640	60.60	13.444	5.00
1.31 (HCP 50)	-20.841	60.40	13.260	5.13
1.5	-23.127	59.60	13.322	4.07
3	-12.579	57.5	7.4916	1.74
5	-14.759	56.5	6.2728	2.43

4.3.2 Protective Material

The filling material can be extended to cover the whole antenna substrate surface for extended protection, as shown in Fig. 4.12. Due to the introduction of filling dielectric, the antenna does not need any special supporting parts around it or around the slabs. This way the structure is more suitable for real-life applications. Table 4.8 summaries the results of this study. The same two filling materials are used, and the results are compared to the air filling case. Again, the effect of the HPC 50 polymer foam on the antenna directivity and resonance behavior is insignificant.

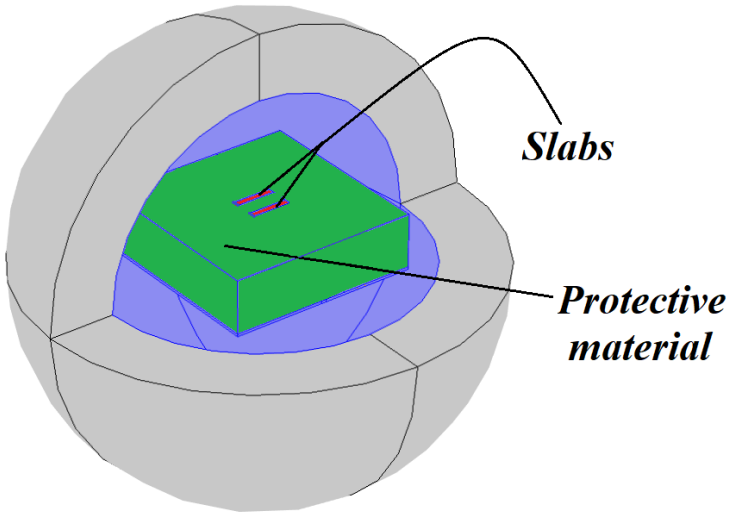

Figure 4.12: Geometry of the DFPR antenna showing protective material.

Table 4.8: Simulation results for different protective materials.

Material Dielectric Constant	**Return Loss (dB)**	**Resonance Frequency (GHz)**	**Directivity (dB)**	**Bandwidth (%)**
1.0	-46.640	60.60	13.444	5.00
1.31 (HCP 50)	-33.938	60.80	12.630	5.75
1.5	-34.199	59.70	13.260	4.7

4.4 Analysis of Results

In the parametric studies of section 4.3 it was observed that the antenna directivity is affected with different degrees and in different ways by the various DFPR parameters. In the following Fig. 4.13,4.14,4.15,4.16, graphical representations of these results are produced. The figures reveal that the antenna directivity

exhibits a peak for certain values. It is more instructive to link these behaviors to the operating (resonance) frequency or the wavelength. Since the parameters are actually distance parameters, wavelength is more appropriate.

Figures 4.17 4.18 4.19 4.20 represent the same results but with wavelength-normalized horizontal axis. The main objective of this representation is to come up with guidelines for the DFPR design that produces the best directivity value. In all of these figures, it is clear that there exists a range of values where directivity is best. It is clear from Fig. 4.17 that directivity peaks at around an effective cavity length of $\lambda/2$. This of course matches with the cavity resonance conditions. From figures 4.18 and 4.19, it can be concluded that best directivity is attained if the slab width and height are both set to around one wavelength. Finally, Fig. 4.20 shows an optimum value for the slab thickness in case of a single slab design. This value corresponds to $\lambda/2$ inside the slab dielectric material. It should be remembered that the wavelength inside any dielectric with dielectric constant ε_r is given by $\lambda/\sqrt{\varepsilon_r}$.

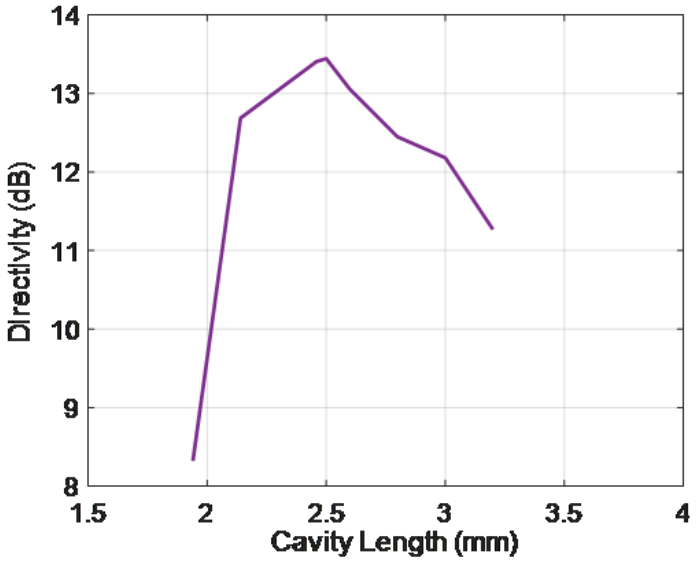

Figure 4.13: Directivity of DFPR antenna vs cavity length.

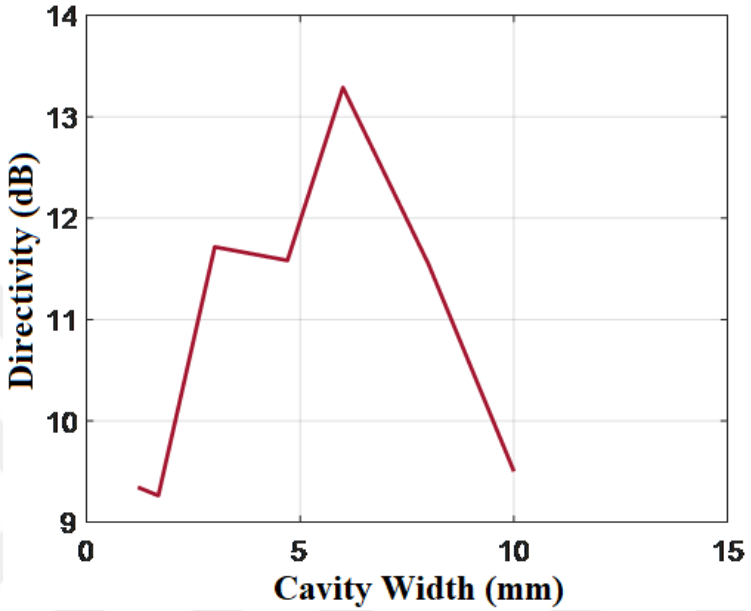

Figure 4.14: Directivity of DFPR antenna vs cavity width.

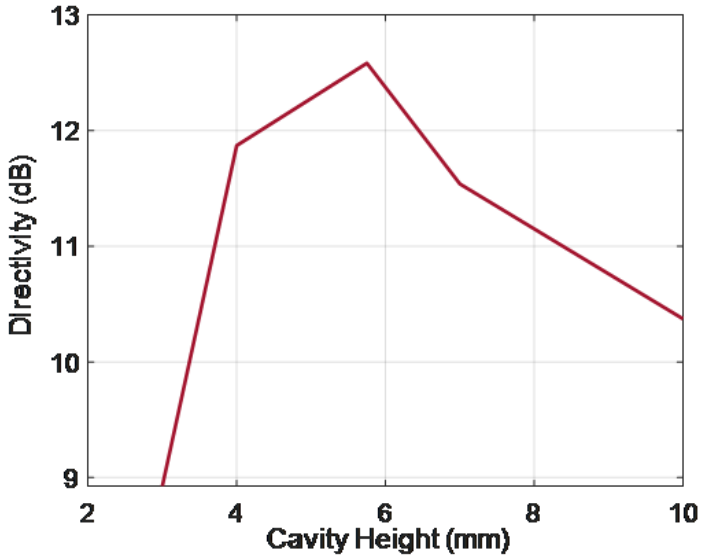

Figure 4.15: Directivity of DFPR antenna vs cavity height.

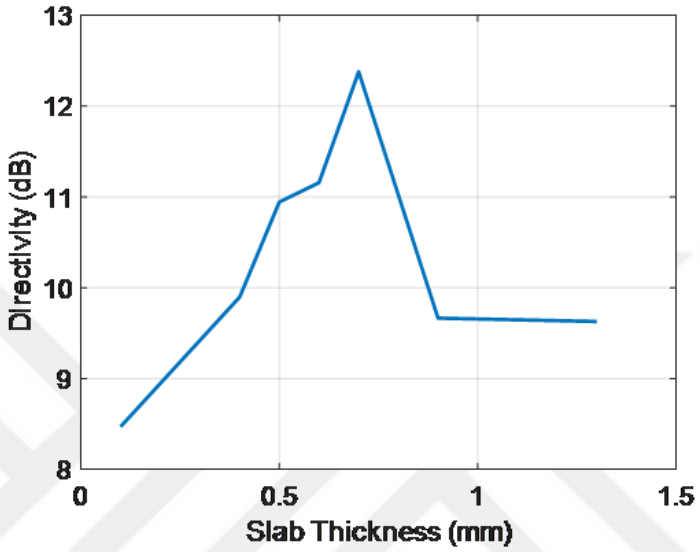

Figure 4.16: Directivity of DFPR antenna vs slab thickness.

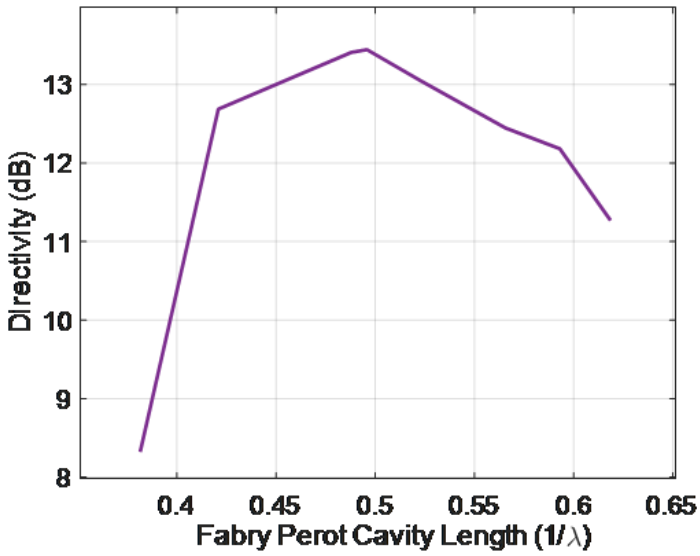

Figure 4.17: Directivity of DFPR antenna vs normalized effective cavity length.

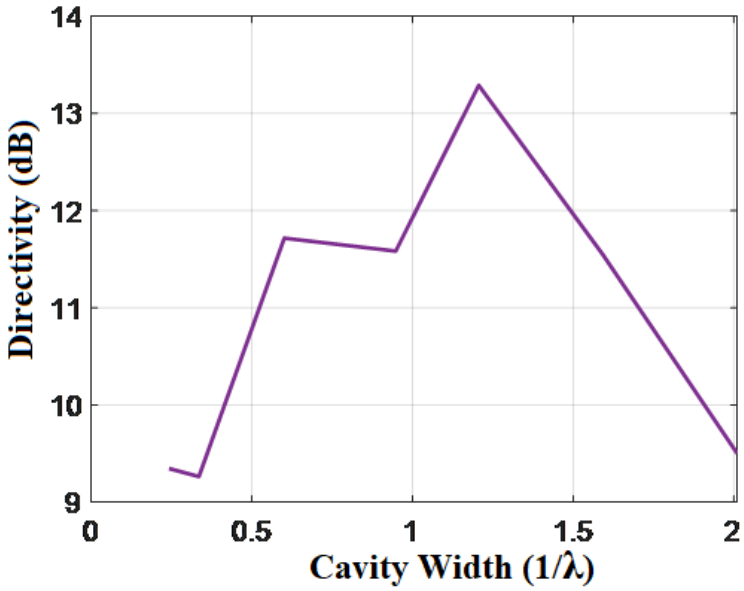

Figure 4.18: Directivity of DFPR antenna vs normalized cavity width.

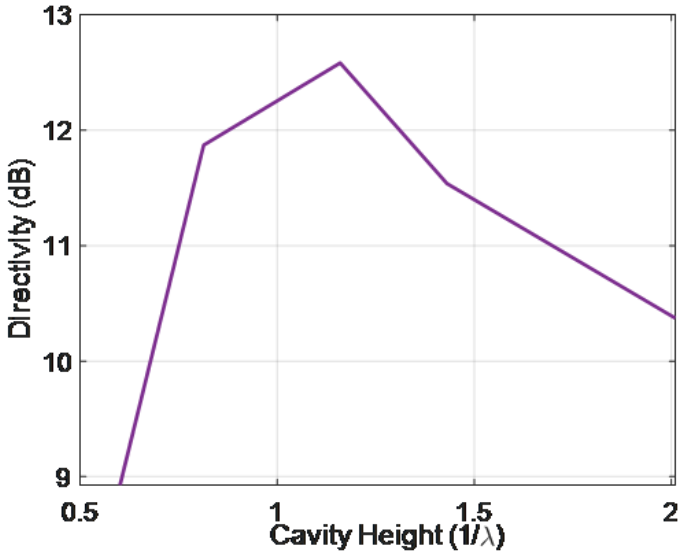

Figure 4.19: Directivity of DFPR antenna vs normalized cavity height.

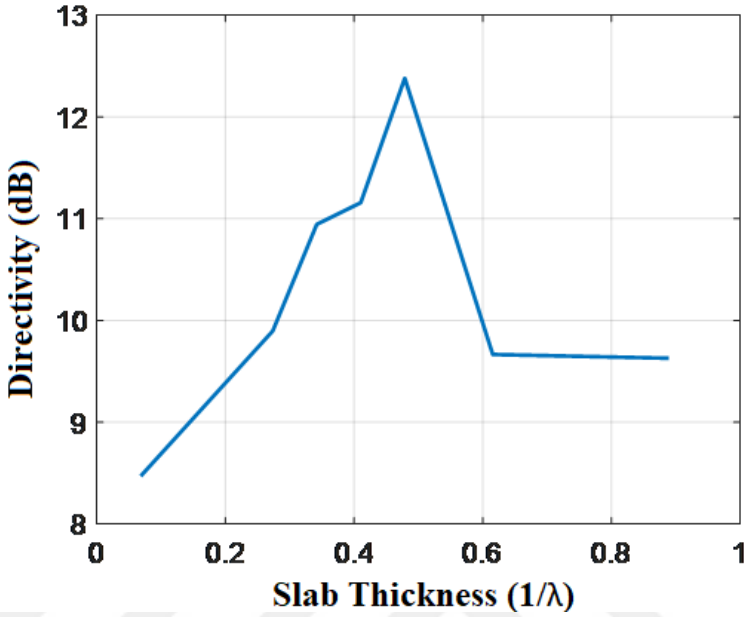

Figure 4.20: Directivity of DFPR antenna vs normalized slab thickness.

4.5 The Proposed DFPR-based Patch Antenna Design

The parametric study and detailed analysis performed earlier have revealed important features of the best DFPR design for enhanced directivity. Fig 4.21 shows a schematic of the different parameters that are involved in the DFPR design. For each of the DFPR parameters, the value that gives the best directivity is selected.

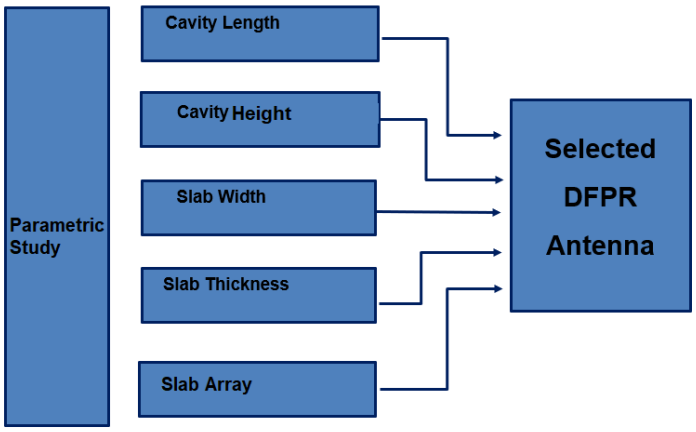

Figure 4.21: Flow chart of design procedure.

The guidelines for the design of a suitable DFPR were discussed separately for each parameter in the previous sections. Table 4.9 gives a summary of the design guideline for each parameter. It also shows the specific values for the DFPR design considering the basic reference antenna parameters.

Table 4.9: Design guideline of DFPR.

DFPR Parameter	**Design Guideline**	**Design Value**
Length	$\lambda_c/2$	2.5mm
Height	λ_c	5.75 mm
Width	λ_c	4.7 mm
Slab thickness	$\lambda_s/2$	0.7 mm
Filling material	$\epsilon_r \approx 1.0$	Air
Array	single	single

The proposed antenna has been designed and analyzed according to the parameters in Table 4.9. Figures 4.22 4.23 4.24 4.21-4.23 show the return loss and radiation patterns of this DFPR-based antenna. The antenna resonates at around 60.6 GHz with a bandwidth of 3 GHz (5%). The directivity value is 13.444 dB. Compared to the reference patch antenna, the radiation pattern in Fig. 4.23

shows a significant improvement in the antenna directivity. It should be noted that this enhancement does not come on the expense of other antenna parameters.

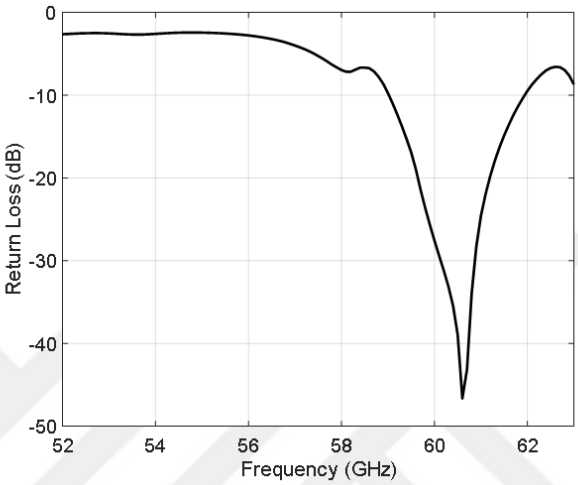

Figure 4.22: Return loss of DFPR antenna.

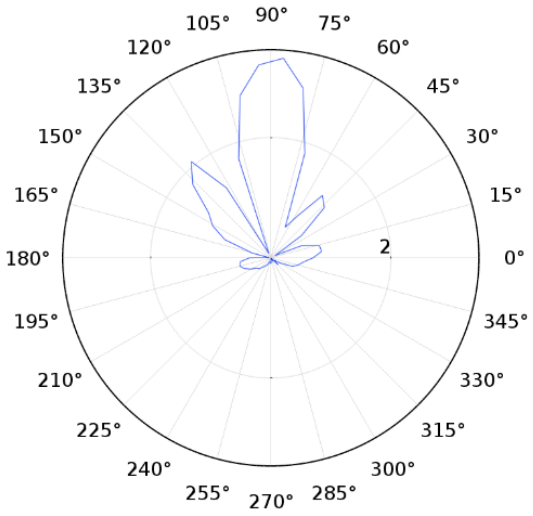

Figure 4.23: 2D radiation pattern of the DFPR antenna.

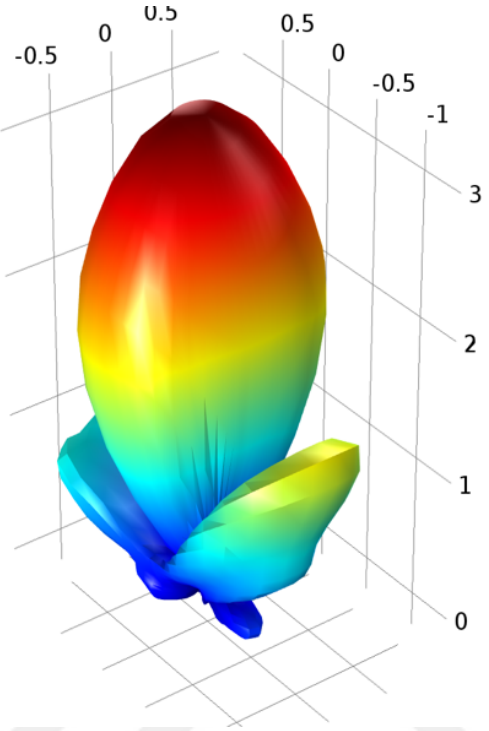

Figure 4.24: 3D radiation pattern of the DFPR antenna.

4.6 Experimental Work

Due to insufficient facilities faced during the writing of this thesis and lack of necessary measurement system at 60 GHz, antenna measurement and fabrication is carried out at 6 GHz, as a proof of concept. 60 GHz directivity improvement method is applied for the same concept at 6 GHz, which is considered to be more feasible. The antenna design parameters for 6 GHz frequency are shown in Table 4.10. These parameters are applied to design a 6 GHz antenna using COMSOL Multi-physics. The obtained results are given below.

Table 4.10: Design parameters of reference antenna at 6 GHz.

Parameter	**Value**
Substrate Thickness	1 mm
Antenna width (W)	15.20 mm
Antenna length (L)	11.60 mm
Feed line width	1.90mm
Feed line length	6.80 mm
Stub width	1.55 mm
Stub length	3.50 mm

Fig. 4.25 shows the return loss curve for the 6 GHz antenna. The antenna resonates at a frequency of 6.26 GHz with a minimum return loss of –36.668dB, which represents an acceptable resonance.

The 2D and 3D-radiation patterns of the reference inset-fed antenna at the resonance frequency are shown in Fig. 4.26(a) and Fig. 4.26(b). The directivity of the antenna was found to be 6.7476 dB. It is clear from Fig. 4.26(a) and Fig. 4.26(b) that the patterns are consistent with a standard microstrip patch antenna.

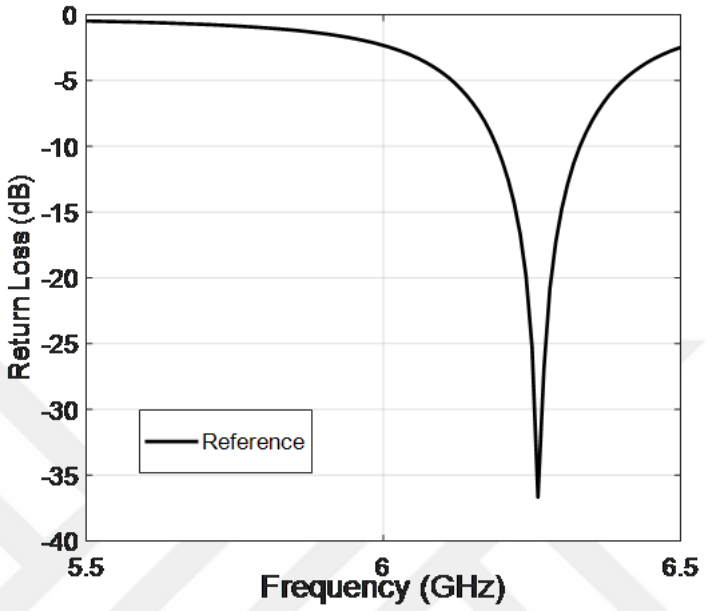

Figure 4.25: Return loss of simulated reference antenna at 6 GHz.

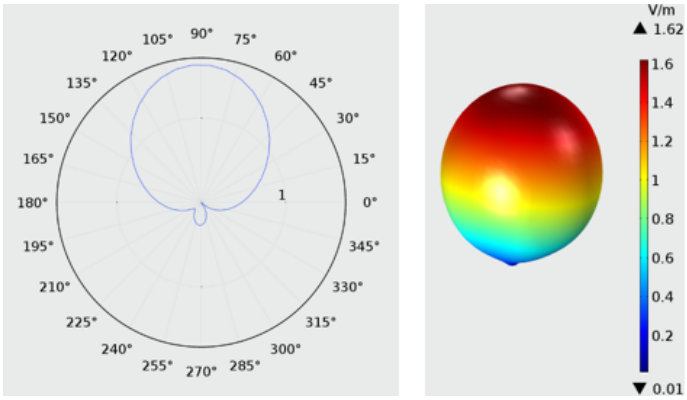

Figure 4.26: Representation of the reference antenna radiation pattern (a) 2D view (b) 3D view.

Table 4.11: Design parameters of DFPR antenna at 6 GHz.

Parameter	**Value**
Substrate Thickness	1 mm
Antenna width (W)	15.20 mm
Antenna length (L)	11.60 mm
Feed line width	1.90mm
Feed line length	54.2 mm
Stub width	1.55 mm
Stub length	3.50 mm

Next, the design and simulation of a dielectric Fabry-Perot resonator antenna is considered. The parameters used for the at 6 GHz operation are as shown in Table 4.11. The slab material is selected to be ceramic with dielectric constant of 6, and the cavity width,length and height are 50 mm, 10 mm, and 50 mm respectively.

Fig. 4.27 shows the return loss curve for the 6 GHz antenna. The antenna resonates at a frequency of 6.37 GHz with a minimum return loss of –46.119 dB. The 2D and 3D-radiation patterns of the DFPR antenna at the resonance frequency are shown in Fig. 4.28(a) and Fig. 4.28(b). The directivity of the antenna was found to be 13.054 dB.

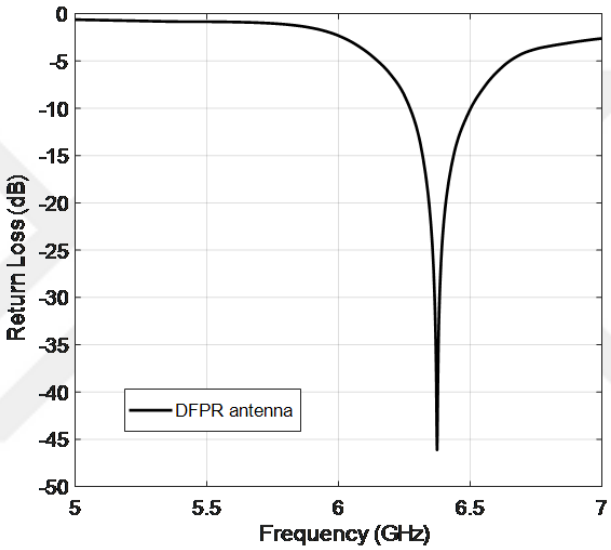

Figure 4.27: Return loss of simulated DFPR antenna.

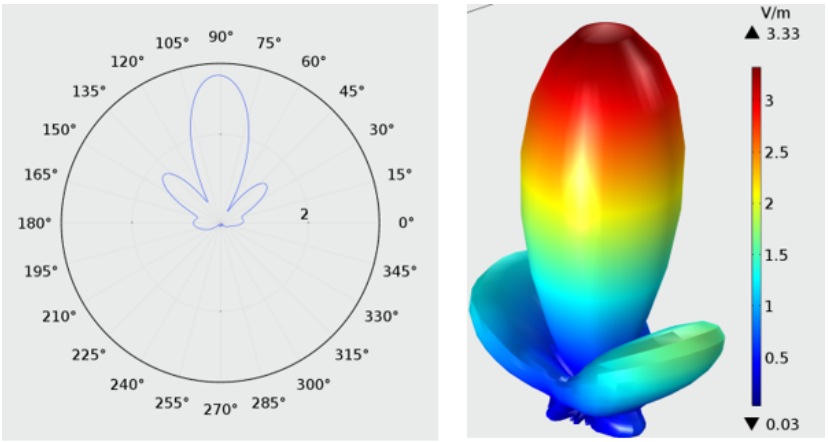

Figure 4.28: Representation of the DFPR antenna radiation pattern (a) 2D view (b) 3D view.

Fig. 4.28 shows that the theorem also verifies at 6 GHz hence the assessment of concept verification is reasonable.

The fabrication of the simulated antennas has been carried out at Istanbul Medipol University facility using the LPKF ProtoMat-D140 PCB fabrication machine. The microstrip patch antennas were fabricated on an FR4 substrate. The following figure shows the production steps of the reference antenna and the Fabry-Perot antenna.

Figure 4.29: Fabrication process of antennas.

Next, the S-parameters of both antennas were measured using the Rohde Schwarz FSH8 – Network Analyzer. The coaxial cables used for measurements are calibrated to 50 ohms impedance to avoid mismatch with the antennas. Fig. 4.30 and Fig. 4.31, respectively, show the return loss results for the fabricated reference and fabricated DFPR antennas.

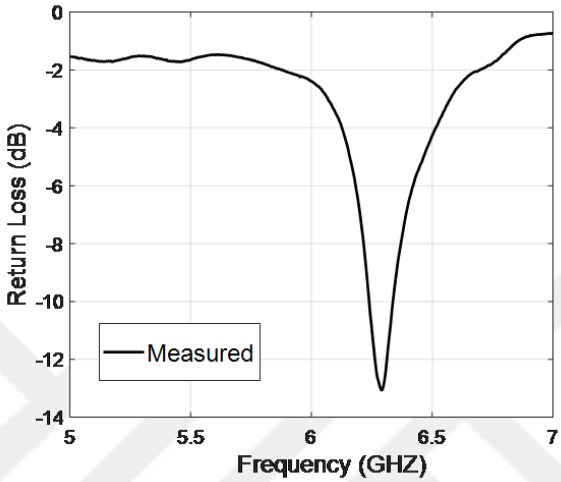

Figure 4.30: Measured return loss of reference antenna at 6 GHz.

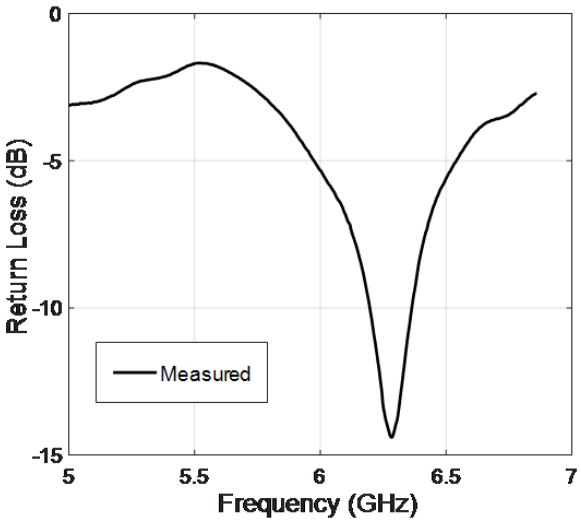

Figure 4.31: Measured return loss of DFPR antenna at 6 GHz.

The fabricated reference antenna has a minimum return loss at -13.10 dB corresponding to a resonance frequency at 6.29 GHz. For the fabricated DFPR antenna, the minimum return loss is at -14.40 dB corresponding to a resonance frequency at 6.28 GHz.

4.6.1 Measurement-1: Slabs at λ distance

The radiation pattern measurements of the reference antenna and the DFPR antenna, shown in Fig. 4.32, are carried out at TUBITAK Informatics and Information Security Research Center in Antenna Test and Research Laboratory using anechoic far-field chamber facility. The radiation patterns of the antennas give comparative estimations about the improvement in directivity.

Figure 4.32: The photograph of the reference and DFPR antennas.

The most important features of the anechoic chamber are being electromagnetically shielded such that the prevention of the reflections inside the chamber is achieved. The black pyramids shown in Fig. 4.35 suppress the reflections from surrounding objects, hence the measurement of radiation properties of the antenna becomes possible. The system could perform measurements from 1 GHz up to 40 GHz. This is considerably a wide band. Here it is possible to measure large antennas like satellite communication antennas or small-sized millimeter wave antennas.

The preceding results clearly provide the required proof of concept. Fig. 4.33 and 4.34 show the comparison between the simulated and measured return loss for both the reference antenna and the DFPR antenna. The agreement is very good as far as the resonance location is concerned. The slight deviation in resonance frequency in the DFPR antenna is due to the uncertainty in the dielectric constant value of the slabs. The low quality of the resonance in the measurement case is due to a slight inevitable impedance mismatch caused by imperfections of the fabrication process. The return loss values for the simulated and the fabricated DFPR antennas show differences for the same reasons mentioned above and plus the effect of the glue material that is used for sticking the slabs to the antenna.

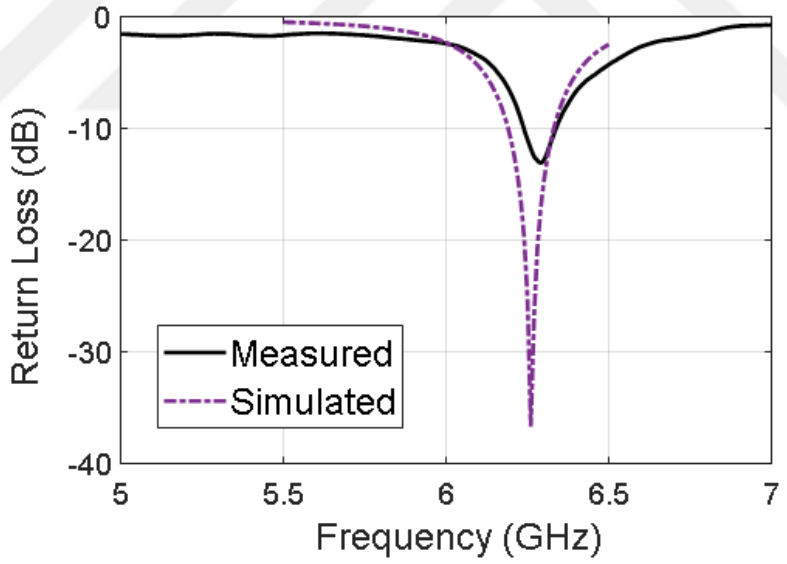

Figure 4.33: Return loss comparison for simulated and measured reference antennas.

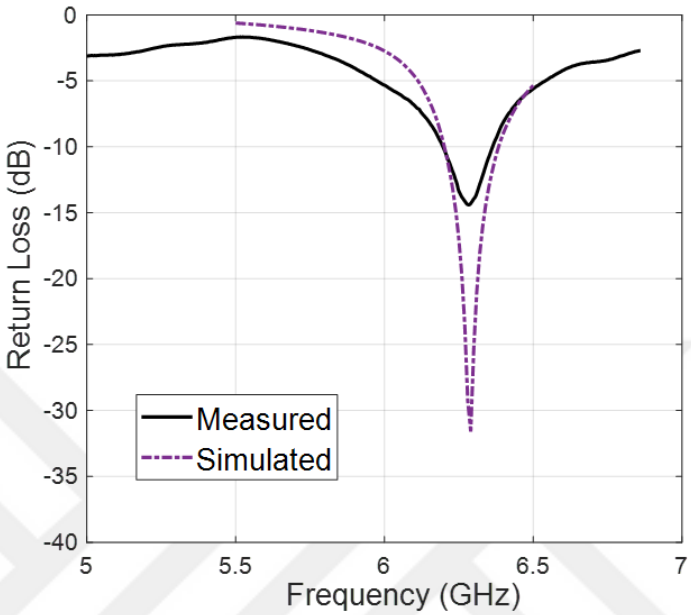

Figure 4.34: Return loss comparison for simulated and measured DFPR antennas.

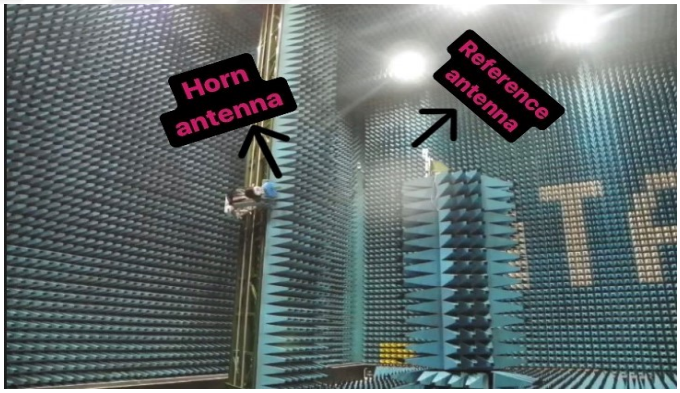

Figure 4.35: The photograph of the reference antenna on the measurement fixture.

It is interesting to check second harmonic ($m = 2$) resonance of the cavity. In this case, the slabs are placed one wavelength apart.

First, the reference antenna is set to the tower system as shown in Fig. 4.35. A horn antenna which is labeled in Fig. 4.35, known to have wide bandwidth, is set as a receiver to the opposite side of the reference antenna. Measurements at angles from -180 to 180 degrees in steps of 0.45 degrees are taken. The same procedure is repeated for the DFPR antenna. Fig. 4.36 below shows the DFPR antenna without (left) and with (right) protective material.

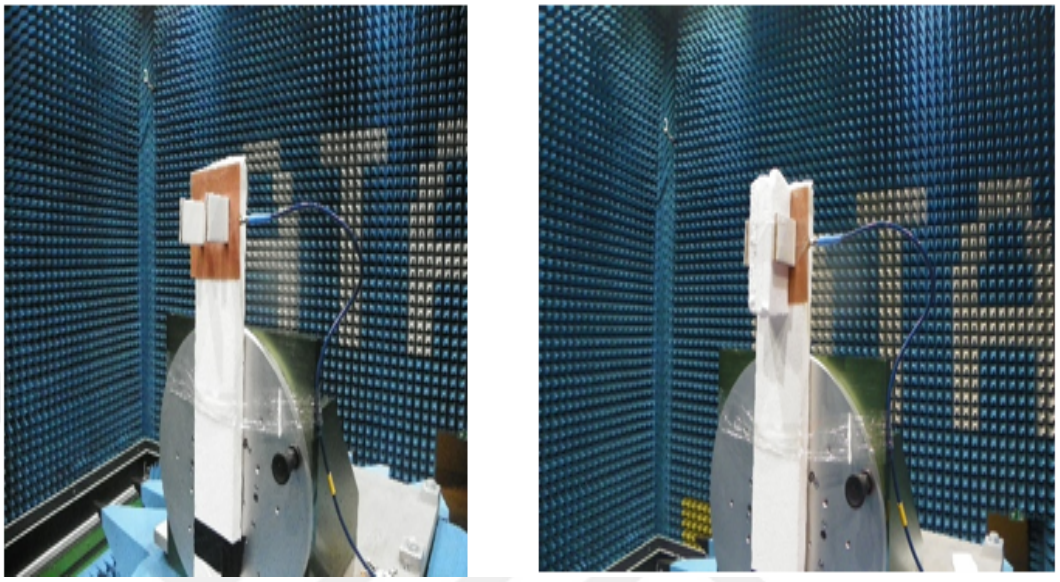

Figure 4.36: The photograph of the DFPR antenna without (left) and with (right) protected material.

Figures 4.33- 4.36 present the radiation pattern measurements for the reference and the DFPR antennas (with and without protective filling material), at 6.3 GHz and 6.4 GHz frequencies.

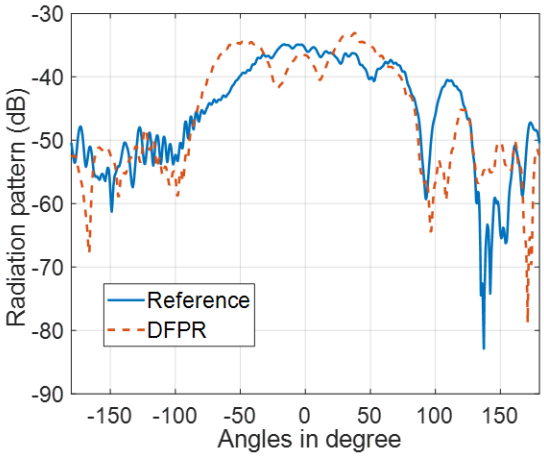

Figure 4.37: Measured radiation patterns comparison at 6.3 GHz

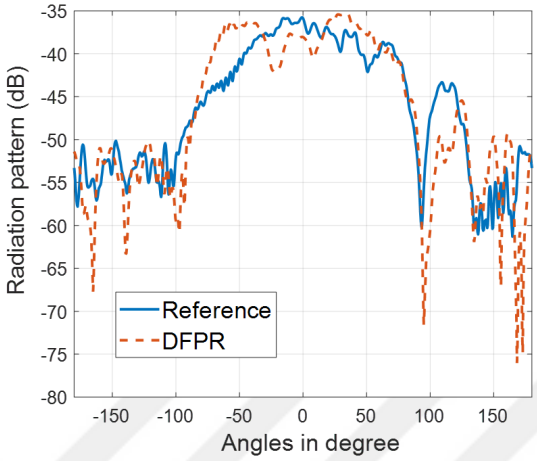

Figure 4.38: Measured radiation patterns comparison at 6.4 GHz.

It is obvious from the Figs. 4.37 to 4.38 that the antenna directivity has improved with the application of the DFPR concept considering the maximum points where DFPR has higher value than the reference antenna. The two peaks in the radiation pattern coincide with the peaks of the cavity mode (second harmonic). The improvement of the directivity is clearer in Fig. 4.37 at around 90° where it points the maximum value of radiation pattern of the antenna in simulation result Fig. 4.28(a). Fig. 4.37 has the closest frequency value to the resonance of the fabricated antenna. The difference between maximum points for the measured DFPR antenna directivity and for the measured reference antenna directivity ranges between 2.79 dB and 4.99 dB. The two lobes in the patterns show the second harmonic case of the radiation because in this measurement the DFPR slabs were placed in one wavelength distance of the cavity.

4.6.2 Measurement-2: Slabs at $\lambda/2$ distance

Next radiation pattern measurements of the reference antenna and the DFPR antenna, shown in Fig. 4.39, are carried out at TUBITAK National Metrology Institute anechoic chamber facility. The radiation patterns of the antennas give comparative estimations about the improvement in the directivity.

Figure 4.39: The photograph of the measurement fixture.

First the reference antenna is placed to the measurement setup and a horn antenna operating in a wideband at 6 GHz is placed right across to the antenna. Measured values are recorded at each 10° angles from 0° to 360° for ϕ=0°. Same procedure is repeated for the DFPR antenna and to the DFPR antenna with the protective material. Fig. 4.40 shows the designed reference, DFPR and DFPR with protective material antenna images and Fig. 4.41 shows the S_{11} result for the new DFPR antenna in which slabs are placed half-wavelength apart.

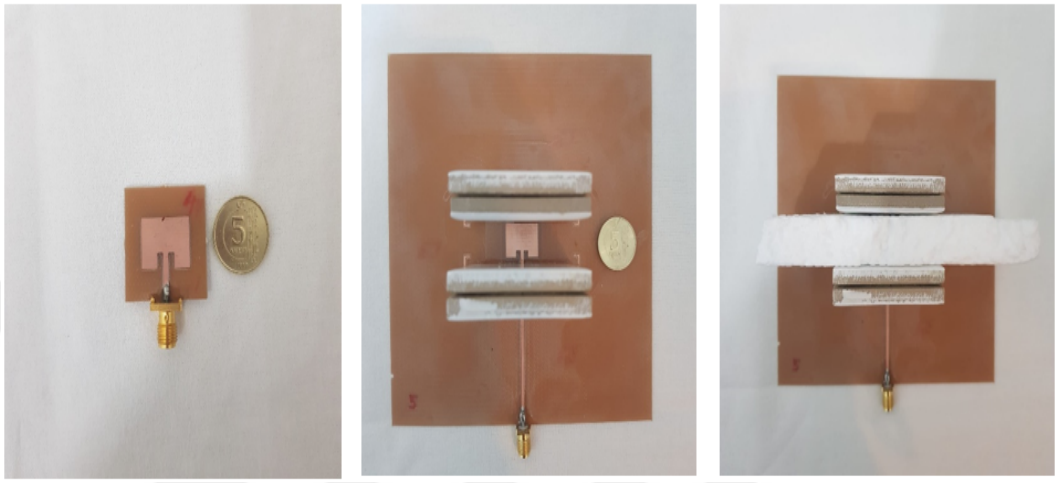

Figure 4.40: The photograph of the measured antennas,the reference antenna(left),the DFPR antenna(middle), and the DFPR antenna with foam(right).

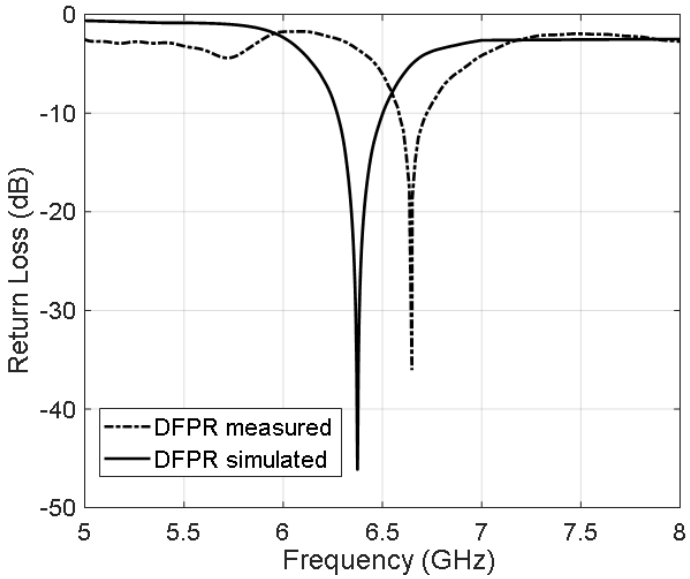

Figure 4.41: The return loss of DFPR simulated and DFPR measured antennas.

Measurement results for the reference and DFPR antenna at $\phi = 0$ are shown in Fig. 4.42 and in Fig. 4.43.

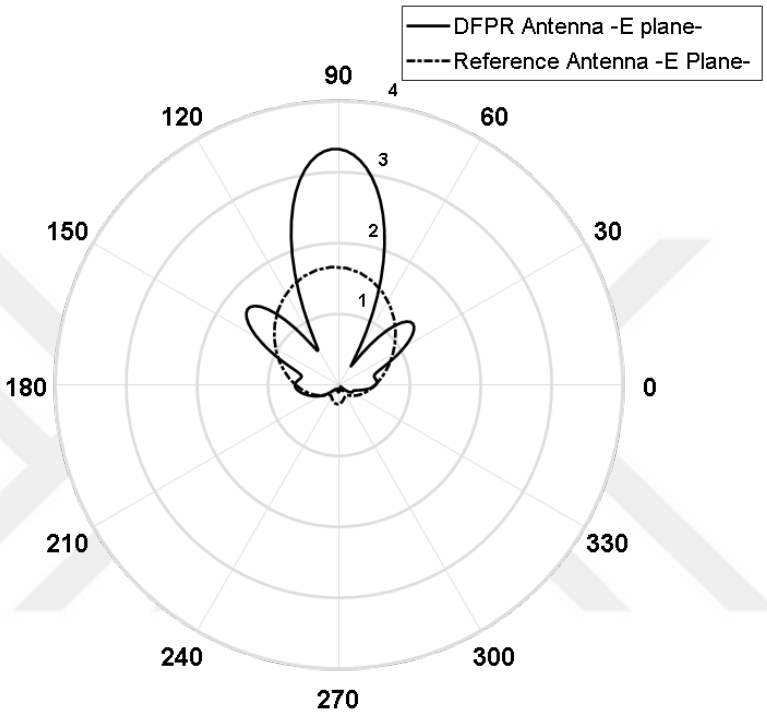

Figure 4.42: The radiation pattern of the simulated reference antenna and DFPR antenna.

Fig. 4.43 shows the normalized measured field pattern of DFPR and reference antennas. It demonstrates that implementing the DFPR to the reference antenna concentrates more energy in one direction in preference to other directions.

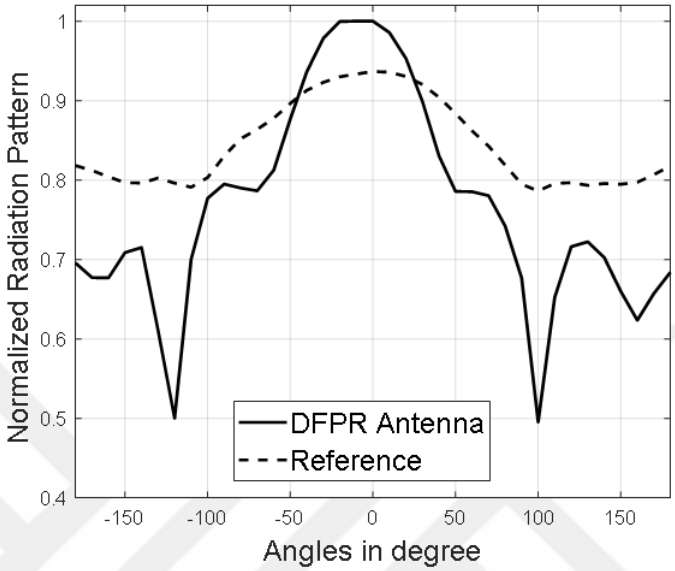

Figure 4.43: The normalized radiation pattern of the measured reference antenna and DFPR antenna in angles.

Fig. 4.44 is generated by self-normalizing each of the two patterns to illustrate the narrowing of the bandwidth as a result of the application of this method. It is obvious that the focusing caused by the DFPR method is large.

The implemented simulations are verified by the measurements. Experimental results of DFPR antenna design demonstrate that this novel approach facilitates enhancement in antenna directivity. However, there are some imperfections that reduce the quality of the measurement results. In the following paragraphs, some of these imperfections are discussed.

There are lots of reports characterizing the dielectric constant of FR4, but due to different manufacturers exact information about the dielectric constant is not available. Known dielectric constant value for the FR4 substrates varies between 4.2 and 6.4. But high frequency can cause changes in the standard dielectric constant range, and other values may be obtained. This ambiguity should be considered in the analysis of the experimental result.

Ready ceramic (porcelain) bricks which have specific dimensions that are not

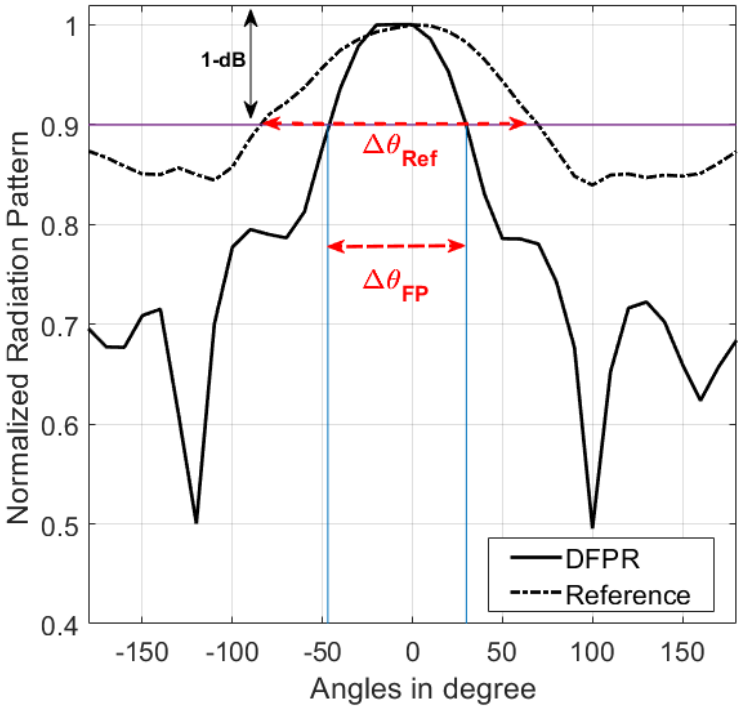

Figure 4.44: The self-normalized radiation pattern of the measured reference antenna and DFPR antenna in angles.

the same with the design parameters are used. To make them same dimensions these slabs are glued to each other to make the required thickness. The glue which is used for sticking the slabs to each other and also attaching the slabs to the substrate can affect the overall response of the antenna. Also the specifications of the slab material are only approximate. It is known that ceramic (porcelain) has dielectric constant between 4.5 and 6.7. In this work dielectric constant value is taken roughly 6.

Another important imperfection factor is the placement of slabs. Although fine adjustments are made to the placement of the slabs and attention paid for the placement very precisely, their position was not same as how it should be. This is another important factor which raises points about possible errors in the measurement result.

Chapter 5

SUMMARY AND CONCLUSIONS

The 60 GHz frequency band can offer a favorable solution for the ever-increasing demand on bandwidth. To overcome the severe atmospheric absorption problem at this frequency band, a detailed account of this absorption as well as a new strategy in antenna design are required. In this thesis, both issues are addressed. A new frequency-dependent material model of the atmosphere at the 60 GHz frequency band is formulated and a new Fabry-Perot-based patch antenna design for directivity enhancement is proposed and implemented. The following sections give a summary of the work done in this dissertation, the major contributions, conclusions and a few ideas for future work.

5.1 Summary and Thesis Contributions

The research work done in this thesis aimed at tackling the atmospheric absorption problem in the 60 GHz frequency band from two aspects; one to quantify the absorption through a material model and one to improve the directivity of a basic patch antenna. The following is a summary of the different activities done

in this thesis including, analytical, simulation and experimental activities.

- A frequency-dependent material model based on the Lorentz pole formulation has been developed for the frequency band 40-80 GHz. Experimental data for the specific attenuation in this band were gathered from recent and reliable sources as a reference. These data were converted to the complex dielectric function and then fitted to standard Lorentzian poles. Many attempts were made to produce an acceptable fit using multi Lorentzian poles.

- A time-domain wave propagation simulator incorporating the developed atmospheric material model was built. The simulator was based on the solution of Maxwell's equations utilizing the finite-difference time-domain method. The frequency-dependent material model was incorporated through an additional differential equation for the polarization vector. This additional auxiliary differential equation (ADE) is solved concurrently with Maxwell's equations using the general algorithm.

- The basic time-domain simulator was empowered with rotating boundaries to allow for extended propagation distances. This way, the numerical dispersion was reduced by choosing a small spatial step, and the computational requirements were made reasonable.

- Extensive numerical experiments were performed to validate the material model. This was achieved through different propagation distances. A propagation distance of one kilometer was also achieved.

- Time-domain as well as frequency-domain field and power analysis were done on the resulting numerical data.

- Verifications of the accuracy of the developed atmospheric material model were performed as compared to the reference experimental data in literature.

- A reference patch antenna for the 60 GHz band was theoretically designed and simulated using COMSOL. Many different variations and simulations

were performed to arrive at an acceptable operation of this reference antenna including the design of the feeding method (inset feeding) for optimum matching.

- A dielectric resonator based on the Fabry-Perot cavity was introduced within the antenna environment. Several simulations were done to observe the effect as well as the suitable placement of the cavity.

- Once the effective positioning was identified, a parametric study of the size and location of the dielectric resonator were carried out. A substantial amount of data representing the operation of the antenna have been collected, including directivity, bandwidth and resonance behavior.

- The generated simulation data have been analyzed to arrive at an overall understanding of the Fabry-Perot-based antenna, and to verify the FP concept.

- Several reference and DFPR antennas have been fabricated for the 6 GHz frequency-band, where the measurement conditions were more favorable. Measurements have been performed twice, first the second harmonic and then the first harmonic cases have been demonstrated. The measurement results have proved the concept's suitability at 6 GHz. Using the described DFPR-based antenna method, the directivity of the antenna has been improved in a simpler way than the most current methods used so far.

5.2 Conclusions

The following points can be concluded from the research work carried out in this thesis.

- The developed analytical material model of the atmosphere at the 60 GHz frequency band gives an accurate representation of the attenuation and dispersion that propagating electromagnetic waves suffer. The model has

been verified against published experimental data. It has been shown that improving the fitting process by adding more Lorentzian poles can improve the accuracy of the model.

- Unlike empirical models, the proposed analytical model of the atmosphere fits very naturally in standard numerical electromagnetic simulators such as the FDTD and the FEM methods. It has been incorporated in this thesis in the FDTD method using the ADE technique, where the polarization field was introduced.

- The rotating boundary conditions proved to be very effective in the solution of long-distance problems. It has been used in this thesis for hundreds of meters of propagation. These conditions have to be modified for cases where reflections are present within the computations window.

- The simulation as well as the experimental work have shown that the concept of a dielectric resonator can significantly affect and enhance the directivity of a basic patch antenna without compromising other antenna properties such as gain and efficiency.

- The concept of directivity enhancement using a dielectric resonator is based on matching the cavity resonance of the Fabry-Perot structure to the antenna resonance. In this way, the radiated fringing fields from the patch antenna are efficiently coupled to the resonator's fundamental mode. This cavity fundamental mode is then refocused in a given direction of propagation and hence improving the directivity.

- The dimensions of the Fabry-Perot cavity should be set for optimum matching with the antenna resonance. Most importantly, the cavity length should be set to satisfy the $\lambda/2$ condition for resonance, where λ is the wavelength that corresponds to the antenna resonance frequency. Because the cavity is dielectric a slight correction is required depending on the extent of the penetration of the fields into the cavity dielectric walls. If the dielectric constant of the cavity walls is high, the amount of correction is negligible.

- The optimum values for the Fabry-Perot cavity width and height are one wavelength. These values produce the best directivity results. However,

it was found that these dimensions are not crucial factors for directivity enhancement.

- The thickness of the cavity dielectric slabs has little effect on directivity because of the short penetration depth of the field in case of high dielectric constant.
- Simulations have shown that inserting a low dielectric constant protective material for the on-substrate resonator does not alter the directivity levels of the structure. This protective material might be needed for the integrity of the structure.
- Experimental work for antennas in the 60 GHz band is quite challenging. From fabrication point of view, special printed circuit (PC) etching tools are required to produce the antenna small dimensions as accurately as possible. Also, common PCs are not suitable for this frequency band due to high losses.
- A proof of concept has been carried out. The simulated DFPR antennas at 60 GHz frequency band have been designed and measured at 6 GHz frequency. DFPR antenna implementation for 6 GHz showed an increase in directivity.

5.3 Future Work

The work done in this thesis opens several directions for further research on different fronts including the atmospheric propagation model as well as directivity enhancement. Possible extensions can be in the range of applicability of the time-domain propagation model as well as the effect of dielectric resonators built around the patch antenna. Possible specific recommendations for extending this research study are as follows.

- The proposed analytical model of the atmospheric effects on electromagnetic waves in the 60 GHz frequency band can be even more accurate by

improving the fitting process. This may involve adding more Lorentzian poles. The direct effect of this improvement is extra computational cost.

- Extension of the atmospheric material model to other altitudes and weather conditions including pressure and temperature. These effects can be reflected in the Lorentz poles in a similar procedure used in this thesis.

- A versatile material model of the atmosphere can also be embedded in standard commercial electromagnetic simulators.

- The time-domain simulator can be extended to multidimensional situations that include buildings, terrain and other scatterers. Such an extension will provide a powerful tool that assists in positioning of ground as well as airborne communication facilities.

- New designs and variations of the Fabry-Perot concept to improve directivity can be investigated. One such concept is the High Contrast Grating (HCG) technique. The HCG provides an alternative way of focusing electromagnetic waves and hence improve antenna directivity.

Bibliography

[1] B. V. Quang, R. V. Prasad, and I. Niemegeers, "A survey on handoffs — lessons for 60 ghz based wireless systems," *IEEE Communications Surveys Tutorials*, vol. 14, pp. 64–86, First 2012.

[2] M. Peter, W. Keusgen, and J. Luo, "A survey on 60 ghz broadband communication: Capability, applications and system design," in *2008 European Microwave Integrated Circuit Conference*, pp. 1–4, Oct 2008.

[3] F. Hu, *Opportunities in 5G networks: A research and development perspective*. CRC press, 2016.

[4] T. Yilmaz and O. B. Akan, "State-of-the-art and research challenges for consumer wireless communications at 60 ghz," *IEEE Transactions on Consumer Electronics*, vol. 62, pp. 216–225, August 2016.

[5] Z. Cao, X. Zhao, F. Soares, N. Tessema, and A. Koonen, "38-ghz millimeter wave beam steered fiber wireless systems for 5g indoor coverage: architectures, devices, and links," *IEEE Journal of Quantum Electronics*, vol. 53, no. 1, pp. 1–9, 2016.

[6] A. S. Hamza, J. S. Deogun, and D. R. Alexander, "Wireless communication in data centers: A survey," *IEEE communications surveys & tutorials*, vol. 18, no. 3, pp. 1572–1595, 2016.

[7] A. Al-Sayadi, H. Vettikalladi, and M. A. Alkanhal, "Millimeter wave antenna based on siw technology for wlan/wpan 5g networks at 60ghz," in *2017 International Conference on Electrical and Computing Technologies and Applications (ICECTA)*, pp. 1–4, IEEE, 2017.

[8] N. Regimbal, Y. Deval, F. Badets, and J.-B. Begueret, "Limitations of fractional synthesizers for 60 ghz wpans: A survey," in *2009 Joint IEEE North-East Workshop on Circuits and Systems and TAISA Conference*, pp. 1–4, IEEE, 2009.

[9] R. C. Daniels, J. N. Murdock, T. S. Rappaport, and R. W. Heath, "60 ghz wireless: Up close and personal," *IEEE Microwave magazine*, vol. 11, no. 7, pp. 44–50, 2010.

[10] R. A. Bohlander, R. W. McMillan, and J. J. Gallagher, "Atmospheric effects on near-millimeter-wave propagation," *Proceedings of the IEEE*, vol. 73, no. 1, pp. 49–60, 1985.

[11] N. P. Narekar and D. M. Bhalerao, "A survey on obstacles for 5g communication," in *2015 International Conference on Communications and Signal Processing (ICCSP)*, pp. 0831–0835, IEEE, 2015.

[12] W. J. Allen, M. E. Gorzynski, P. G. Howard, and P. J. McClellan, "Image display system and method," Apr. 18 2006. US Patent 7,030,894.

[13] W. L. Stutzman and G. A. Thiele, "Antenna theory and design, john w iley & sons," *Inc., New York*, 1998.

[14] A. F. Oskooi, D. Roundy, M. Ibanescu, P. Bermel, J. D. Joannopoulos, and S. G. Johnson, "Meep: A flexible free-software package for electromagnetic simulations by the fdtd method," *Computer Physics Communications*, vol. 181, no. 3, pp. 687–702, 2010.

[15] C. Multiphysics, "v. 5.3 a. www. comsol. com. comsol ab, stockholm," 2018.

[16] K. Yee, "Numerical solution of initial boundary value problems involving maxwell's equations in isotropic media," *IEEE Transactions on antennas and propagation*, vol. 14, no. 3, pp. 302–307, 1966.

[17] A. Taflove and S. C. Hagness, *Computational electrodynamics: the finite-difference time-domain method*. Artech house, 2005.

[18] D. Makarov, M. Y. Tretyakov, and P. Rosenkranz, "60-ghz oxygen band: Precise experimental profiles and extended absorption modeling in a wide temperature range," *Journal of Quantitative Spectroscopy and Radiative Transfer*, vol. 112, no. 9, pp. 1420–1428, 2011.

[19] ITU, "International telecommunication union, attenuation by atmospheric gases, recommendation itu-r p.676-9, 02/2012.," pp. 676–9, 2012.

[20] H. J. Liebe, "Mpm—an atmospheric millimeter-wave propagation model," *International Journal of Infrared and millimeter waves*, vol. 10, no. 6, pp. 631–650, 1989.

[21] M. Y. Tretyakov, M. Koshelev, V. Dorovskikh, D. Makarov, and P. Rosenkranz, "60-ghz oxygen band: precise broadening and central frequencies of fine-structure lines, absolute absorption profile at atmospheric pressure, and revision of mixing coefficients," *Journal of molecular spectroscopy*, vol. 231, no. 1, pp. 1–14, 2005.

[22] F. J. Wentz and T. Meissner, "Atmospheric absorption model for dry air and water vapor at microwave frequencies below 100ghz derived from spaceborne radiometer observations," *Radio Science*, vol. 51, no. 5, pp. 381–391, 2016.

[23] D. V. Grishin, D. Y. Danilov, and L. V. Kurakhtenkov, "Use of itu-r recommendations in calculating tropospheric signal attenuation in the simulation modeling problems of satellite systems," in *2017 Systems of Signal Synchronization, Generating and Processing in Telecommunications (SINKHROINFO)*, pp. 1–4, IEEE, 2017.

[24] A. C. Valdez, *Analysis of atmospheric effects due to atmospheric oxygen on a wideband digital signal in the 60 GHz band.* PhD thesis, Virginia Tech, 2001.

[25] A. Chinmayi, M. Vasanthi, and T. R. Rao, "Performance evaluation of rf based inter satellite communication link at 60 ghz," in *2016 International Conference on Wireless Communications, Signal Processing and Networking (WiSPNET)*, pp. 59–64, IEEE, 2016.

[26] J. G. Powers, J. B. Klemp, W. C. Skamarock, C. A. Davis, J. Dudhia, D. O. Gill, J. L. Coen, D. J. Gochis, R. Ahmadov, S. E. Peckham, *et al.*, "The weather research and forecasting model: Overview, system efforts, and future directions," *Bulletin of the American Meteorological Society*, vol. 98, no. 8, pp. 1717–1737, 2017.

[27] A. E. Barrios, "A terrain parabolic equation model for propagation in the troposphere," *IEEE Transactions on Antennas and Propagation*, vol. 42, no. 1, pp. 90–98, 1994.

[28] J. R. Kuttler and G. D. Dockery, "Theoretical description of the parabolic approximation/fourier split-step method of representing electromagnetic propagation in the troposphere," *Radio science*, vol. 26, no. 2, pp. 381–393, 1991.

[29] H. Zhou, A. Chabory, and R. Douvenot, "A 3-d split-step fourier algorithm based on a discrete spectral representation of the propagation equation," *IEEE Transactions on Antennas and Propagation*, vol. 65, no. 4, pp. 1988–1995, 2017.

[30] C. A. Balanis, "Advanced engineering electromagnetics, john willey & sons," *Inc., New York*, 1989.

[31] M. A. Alsunaidi and A. A. Al-Jabr, "A general ade-fdtd algorithm for the simulation of dispersive structures," *IEEE Photonics Technology Letters*, vol. 21, no. 12, pp. 817–819, 2009.

[32] M. Arvas and M. Alsunaidi, "Analysis of oxygen absorption at 60 ghz frequency band," in *2019 IEEE International Symposium on Antennas and Propagation and USNC-URSI Radio Science Meeting*, pp. 2127–2128, IEEE, 2019.

[33] M. Arvas and M. Alsunaidi, "A multi-pole model for oxygen absorption of 60 ghz frequency band communication signals," *book of*, p. 92.

[34] A. Taflove and S. Hagness, "Computational electrodynamics: The finite-difference time-domain method, (artech house, norwood, 2000); ks kunz and rj luebbers," *The Finite Difference Time Domain Method for Electromagnetics*, 1993.

[35] G. V. Trentini, "Partially reflecting sheet arrays," *IRE Transactions on Antennas and Propagation*, vol. 4, no. 4, pp. 666–671, 1956.

[36] A. P. Feresidis and J. Vardaxoglou, "High gain planar antenna using optimised partially reflective surfaces," *IEE Proceedings-Microwaves, Antennas and Propagation*, vol. 148, no. 6, pp. 345–350, 2001.

[37] Z. Liu, W. Zhang, D. Fu, Y. Gu, and Z. Ge, "Broadband fabry-perot resonator printed antennas using fss superstrate with dissimilar size," *Microwave and Optical Technology Letters*, vol. 50, no. 6, pp. 1623–1627, 2008.

[38] Y. J. Lee, J. Yeo, R. Mittra, and W. S. Park, "Design of a high-directivity electromagnetic band gap (ebg) resonator antenna using a frequency-selective surface (fss) superstrate," *Microwave and Optical Technology Letters*, vol. 43, no. 6, pp. 462–467, 2004.

[39] J. Huang, "Microstrip reflectarray," in *Antennas and Propagation Society Symposium 1991 Digest*, pp. 612–615, IEEE, 1991.

[40] J. Vaughn, "The fabry-perot interferometer: History, theory, practice and applications," *Bristol, PA: Adam Hilger*, 1989.

[41] Z.-g. Liu, "Recently progress in high gain fabry-perot resonator antenna," in *2016 IEEE MTT-S International Microwave Workshop Series on Advanced Materials and Processes for RF and THz Applications (IMWS-AMP)*, pp. 1–3, IEEE, 2016.

[42] S. O. Kasap and R. K. Sinha, *Optoelectronics and photonics: principles and practices*, vol. 340. Prentice Hall New Jersey, 2001.

[43] A. Hosseini, A. T. Almutawa, F. Capolino, and D. R. Jackson, "Wideband single-layer fabry-pérot cavity antenna with a radial variation of the cavity permittivity," in *2017 IEEE International Symposium on Antennas and Propagation & USNC/URSI National Radio Science Meeting*, pp. 2659–2660, IEEE, 2017.

[44] D. Jackson and N. Alexopoulos, "Gain enhancement methods for printed circuit antennas," *IEEE transactions on antennas and propagation*, vol. 33, no. 9, pp. 976–987, 1985.

[45] H. Yang and N. Alexopoulos, "Gain enhancement methods for printed circuit antennas through multiple superstrates," *IEEE Transactions on Antennas and Propagation*, vol. 35, no. 7, pp. 860–863, 1987.

[46] D. Jackson, A. Oliner, and A. Ip, "Leaky-wave propagation and radiation for a narrow-beam multiple-layer dielectric structure," *IEEE Transactions on Antennas and Propagation*, vol. 41, no. 3, pp. 344–348, 1993.

[47] Z. Liu, "Quasi-periodic structure application in fabry-perot resonator printed antenna," in *2008 Asia-Pacific Microwave Conference*, pp. 1–4, IEEE, 2008.

[48] C. Cheype, C. Serier, M. Thèvenot, T. Monédière, A. Reineix, and B. Jecko, "An electromagnetic bandgap resonator antenna," *IEEE Transactions on Antennas and Propagation*, vol. 50, no. 9, pp. 1285–1290, 2002.

[49] A. R. Weily, K. Esselle, T. S. Bird, and B. C. Sanders, "Dual resonator 1-d ebg antenna with slot array feed for improved radiation bandwidth," *IET microwaves, antennas & propagation*, vol. 1, no. 1, pp. 198–203, 2007.

[50] M. U. Afzal and K. P. Esselle, "A low profile flat perforated dielectric beam focusing structure for electromagnetic bandgap resonator antennas," in *2016 IEEE 2nd Australian Microwave Symposium (AMS)*, pp. 31–32, IEEE, 2016.

[51] T. Matsui, H. Yuzawa, N. Hirose, and H. Ohta, "Frequency shift in millimeter wave gaussian beam antenna using two dimensional metal grid mirror," in *IEEE Antennas and Propagation Society International Symposium 1997. Digest*, vol. 4, pp. 2384–2387, IEEE, 1997.

[52] R. Sauleau, G. Le Ray, and P. Coquet, "Parametric study and synthesis of 60-ghz fabry–perot resonators," *Microwave and optical technology letters*, vol. 34, no. 4, pp. 247–252, 2002.

[53] R. Sauleau, P. Coquet, D. Thouroude, and J.-P. Daniel, "Beam focusing using 60 ghz fabry–perot resonators with uniform and non-uniform metal grids," *Electronics Letters*, vol. 39, no. 4, pp. 341–342, 2003.

[54] R. Sauleau, P. Coquet, T. Matsui, and J.-P. Daniel, "A new concept of focusing antennas using plane-parallel fabry-perot cavities with nonuniform mirrors," *IEEE Transactions on Antennas and Propagation*, vol. 51, no. 11, pp. 3171–3175, 2003.

[55] R. Sauleau, P. Coquet, D. Thouroude, J.-P. Daniel, and T. Matsui, "Radiation characteristics and performance of millimeter-wave horn-fed gaussian beam antennas," *IEEE Transactions on Antennas and Propagation*, vol. 51, no. 3, pp. 378–387, 2003.

[56] R. Sauleau, P. Coquet, and T. Matsui, "Low-profile directive quasi-planar antennas based on millimetre wave fabry–perot cavities," *IEE Proceedings-Microwaves, Antennas and Propagation*, vol. 150, no. 4, pp. 274–278, 2003.

[57] S. A. Hosseini, F. Capolino, and F. De Flaviis, "Design of a single-feed 60 ghz planar metallic fabry-perot cavity antenna with 20 db gain," in *2009 IEEE International Workshop on Antenna Technology*, pp. 1–4, IEEE, 2009.

[58] S. A. Hosseini, F. Capolino, and F. De Flaviis, "Single-feed highly-directive fabry-perot cavity antenna for 60 ghz wireless systems: Design and fabrication," in *2010 IEEE Antennas and Propagation Society International Symposium*, pp. 1–4, IEEE, 2010.

[59] S. A. Hosseini, F. De Flaviis, and F. Capolino, "A highly-efficient single-feed planar fabry-pérot cavity antenna for 60 ghz technology," in *Proceedings of the 2012 IEEE International Symposium on Antennas and Propagation*, pp. 1–2, IEEE, 2012.

[60] S. Kabiri, S. A. Hosseini, F. Capolino, and F. De Flaviis, "Gain-bandwidth enhancement of 60ghz single-layer fabry-perot cavity antennas using sparse-array," in *2014 IEEE Antennas and Propagation Society International Symposium (APSURSI)*, pp. 739–740, IEEE, 2014.

[61] S. Kabiri, E. Kornaros, and F. De Flaviis, "A 60 ghz single-layer fabry-perot cavity antennas using sparse array for circularly polarized radiation," in *2015 USNC-URSI Radio Science Meeting (Joint with AP-S Symposium)*, pp. 162–162, IEEE, 2015.

[62] A. Hosseini, F. De Flaviis, and F. Capolino, "A 60 ghz simple-to-fabricate single-layer planar fabry–pérot cavity antenna," *IET Microwaves, Antennas & Propagation*, vol. 9, no. 4, pp. 313–318, 2014.

[63] H. Ostner, E. Schmidhammer, J. Detlefsen, and D. Jackson, "Radiation from dielectric leaky-wave antennas with circular and rectangular apertures," *Electromagnetics*, vol. 17, no. 5, pp. 505–535, 1997.

[64] Y. Lee, X. Lu, Y. Hao, S. Yang, J. R. Evans, and C. G. Parini, "Low-profile directive millimeter-wave antennas using free-formed three-dimensional (3-d) electromagnetic bandgap structures," *IEEE Transactions on Antennas and Propagation*, vol. 57, no. 10, pp. 2893–2903, 2009.

[65] A. Hosseini, F. Capolino, and F. De Flaviis, "Gain enhancement of a v-band antenna using a fabry-pérot cavity with a self-sustained all-metal cap with fss," *IEEE Transactions on Antennas and Propagation*, vol. 63, no. 3, pp. 909–921, 2014.

[66] A. Hosseini, A. T. Almutawa, F. Capolino, and D. R. Jackson, "V-band wideband fabry-pérot cavity antenna made of thick partially-reflective surface," in *2016 IEEE International Symposium on Antennas and Propagation (APSURSI)*, pp. 349–350, IEEE, 2016.

[67] M.-Y. Mi, S.-Q. Zhang, and B.-H. Sun, "A dual-polarized fabry-perot cavity antenna with high gain," in *2017 Sixth Asia-Pacific Conference on Antennas and Propagation (APCAP)*, pp. 1–3, IEEE, 2017.

[68] D. Abbou, T. P. Vuong, R. Touhami, F. Ferrero, D. Hamzaoui, and M. C. Yagoub, "High-gain wideband partially reflecting surface antenna for 60 ghz systems," *IEEE Antennas and Wireless Propagation Letters*, vol. 16, pp. 2704–2707, 2017.

[69] H. Attia, M. L. Abdelghani, and T. A. Denidni, "Wideband and high-gain millimeter-wave antenna based on fss fabry–perot cavity," *IEEE Transactions on Antennas and Propagation*, vol. 65, no. 10, pp. 5589–5594, 2017.

[70] A. Lalbakhsh, U. M. Afzal, P. K. Esselle, and L. S. Smith, "A fabry-perot cavity antenna with a non-uniform permittivity superstrate for v-band applications," in *2018 IEEE Asia-Pacific Conference on Antennas and Propagation (APCAP)*, pp. 223–224, IEEE, 2018.

[71] Q.-Y. Guo and H. Wong, "Wideband and high gain fabry-perot cavity antenna with switched beams for millimeter-wave applications," *IEEE Transactions on Antennas and Propagation*, 2019.

[72] J. Oh, T. Baek, D. Shin, J. Rhee, and S. Nam, "60-ghz cpw-fed dielectric-resonator-above-patch (drap) antenna for broadband wlan applications using micromachining technology," *Microwave and Optical Technology Letters*, vol. 49, no. 8, pp. 1859–1861, 2007.

[73] N. Guérin, S. Enoch, G. Tayeb, P. Sabouroux, P. Vincent, and H. Legay, "A metallic fabry-perot directive antenna," *IEEE Transactions on Antennas and Propagation*, vol. 54, no. 1, pp. 220–224, 2006.

[74] Y. Sun, Z. N. Chen, Y. Zhang, H. Chen, and T. S. See, "Subwavelength substrate-integrated fabry-pérot cavity antennas using artificial magnetic conductor," *IEEE Transactions on Antennas and Propagation*, vol. 60, no. 1, pp. 30–35, 2011.

[75] Y. Ge, C. Wang, and X. Zeng, "Wideband high-gain low-profile 1d fabry-perot resonator antenna," in *2013 Proceedings of the International Symposium on Antennas & Propagation*, vol. 1, pp. 550–552, IEEE, 2013.

[76] N. Wang, J. Li, G. Wei, L. Talbi, Q. Zeng, and J. Xu, "Wideband fabry–perot resonator antenna with two layers of dielectric superstrates," *IEEE Antennas and Wireless Propagation Letters*, vol. 14, pp. 229–232, 2014.

[77] E. Yablonovitch, "Inhibited spontaneous emission in solid-state physics and electronics," *Physical review letters*, vol. 58, no. 20, p. 2059, 1987.

Appendix A

List of Acronyms and Abbreviations

ADE :Auxiliary Differential Equation.

AMC :Artificial Magnetic Conductor.

CAD :Computer-Aided Design.

CEM :Computational Electromagnetic.

CFD :Computational Fluid Dynamics.

CFL :Courant–Friedrichs–Lewy.

DFPR :Dielectric Fabry-Perot Resonator.

ECAD :Electrical Computer-Aided Design.

EHF :Extremely High Frequency.

EM :Electromagnetic.

FDTD :Finite Difference Time Domain.

FEM :Finite Element Methods.

FPC :Fabry-Perot Cavity.

FSS :Frequency Selective Surface.

GBA :Gaussian Beam Antenna.

Gbps :Gigabits per second.

HDTV :High-definition Television.

HFSS :High Frequency Structure Simulator.

ISM :Industrial, Scientific and Medical.

Ka :Kay-A band, 26.5 to 40 GHz.

Ku :Kurtz-under band, 12 to 18 GHz.

LOS :Line of Sigth.

MATLAB :Matrix Laboratory.

Mbps :Megabits per second.

MEEP :Manufacturing Energy Efficiency Program.

MoM :Method of Moments.

NLOS :Non-Line of Sigth.

PRS :Partially Reflected Screen.

RF :Radio Frequency.

DIRECTIVITY ENHANCEMENT OF 60 GHZ MICROSTRIP PATCH ANTENNAS USING DIELECTRIC FABRY-PEROT RESONATORS

ORIGINALITY REPORT

16%	8%	6%	10%
SIMILARITY INDEX	INTERNET SOURCES	PUBLICATIONS	STUDENT PAPERS

PRIMARY SOURCES

1	eprints.kfupm.edu.sa Internet Source	1%
2	dspace5.zcu.cz Internet Source	1%
3	Submitted to Nashville State Community College Student Paper	1%
4	Submitted to Universiti Teknologi Malaysia Student Paper	1%
5	Submitted to University of Birmingham Student Paper	<1%
6	Submitted to University of Sheffield Student Paper	<1%
7	Submitted to Higher Education Commission Pakistan Student Paper	<1%
	Submitted to Universiti Teknologi MARA	